Materials Today Energy 41 (2024) 101528

Contents lists available at ScienceDirect

Materials Today Energy

journal homepage: www.journals.elsevier.com/materials-today-energy/

Multi-dimensional engineering of transition metal dichalcogenides for enhanced performance in fuel cell technologies

Yani Dong [a, c], Zongying Ma [a, c], Isabel Lopez [b], Travis Shihao Hu [b], Qizhi Dong [a, **], Song Liu [a, *]

[a] Institute of Chemical Biology and Nanomedicine (ICBN), State Key Laboratory of Chemo/Biosensing and Chemometrics, College of Chemistry and Chemical Engineering, Hunan University, Changsha, 410082, China
[b] Department of Mechanical Engineering, California State University, Los Angeles, CA, 90032, USA

ARTICLE INFO

Article history:
Received 30 November 2023
Received in revised form
31 January 2024
Accepted 9 February 2024
Available online 13 February 2024

Keywords:
Two-dimensional materials
Different dimensions
Fuel cells
Catalyst
Membrane

ABSTRACT

Fuel cells are considered a highly competitive strategy in the pursuit of sustainable energy, which is crucial for achieving both environmental goals and long-term economic stability. However, challenges such as electrochemical corrosion and fuel penetration still persist in the catalytic layer and electrolyte diaphragm. Tailored nanostructures of two-dimensional (2D) transition metal dichalcogenides (TMDs) hold great potential in addressing these issues due to their wide-ranging modulated properties. Several prominent works are reviewed in this article summarizing the 1D, 2D, and 3D tailored-TMD nanostructures and their assembly techniques. Additionally, the breakthroughs achieved by multi-dimensional nanostructures in addressing limitations such as stacking issues, low conductivity, and loss of active sites in TMDs are discussed. In particular, the effects of manipulating catalysts and electrolyte diaphragms in fuel cells by introducing multi-dimensional nanostructures are highlighted and compared. Finally, the article concludes the challenges that are generally faced in making TMD-based nanostructures a reliable material for the future energy sector.

1. Introduction

The persistent challenges posed by pollution from fossil fuels, carbon emissions, and other environmental issues have prompted reconsidering how to steward the natural environment, which is critical to human survival. There is scientific consensus that global greenhouse gas emissions must be reduced by 45% from 2010 levels by 2030 to limit global warming to 1.5 °C [1]. The transition from environmentally unfriendly fossil fuels to clean renewable energy is inevitable. Governments and researchers worldwide are actively exploring and developing various renewable energy strategies, including the primary energy sources such as solar, wind, and hydropower, as well as the secondary energy sources produced by the primary such as hydrogen and alcohols. Given the intermittent nature of many renewable energy sources (solar, wind, etc.), the development of fuel cells utilizing low-carbon and clean energy-carrying molecules such as hydrogen and methanol as fuel is considered to be a new energy system with great application prospects [2,3]. The mass-produced fuel cell electric vehicles introduced by Hyundai, Toyota and Daimler, boost a driving range of over 500 km and a rapid refueling speed of 3–5 min [4]. Furthermore, these vehicles emit no pollutants such as NO_x or CO, and the only chemical byproduct is pure water when hydrogen is used as a fuel. This makes them an ideal power source for zero emission vehicles [5]. In other words, fuel cells are attractive for their potential to contribute to decarbonization in the portable power applications and transportation sectors.

Fuel cells serve as energy conversion devices, directly converting the chemical energy stored in fuel into electrical energy through electrochemical reactions while continuously discharging the resulting product. The electrodes of fuel cells remain unchanged throughout this process, enabling continuous electricity generation as long as a steady supply of fuel and oxidants is maintained. Consequently, it offers advantages such as high efficiency, low pollution, and minimal noise emissions [6,7]. All fuel cells consist of three fundamental components - anode, cathode, and electrolyte - designed and manufactured in a modular

* Corresponding author.
** Corresponding author.
E-mail addresses: lili2sohu@hnu.edu.cn (Q. Dong), liusong@hnu.edu.cn (S. Liu).
[c] These authors contributed equally to this work.

https://doi.org/10.1016/j.mtener.2024.101528
2468-6069/

structure to facilitate flexible assembly of fuel cell power stations with varying capacities according to specific requirements [8]. In an attempt to make fuel cells efficiency-viable, tremendous research efforts have focused on the iterative development of materials for individual basic units. Two-dimensional (2D) transition metal dichalcogenides (TMDs), with breakthroughs in material preparation and structure customization over the past few decades, are strong candidates for energy conversion.

In recent years, the family of 2D TMDs has undergone continuous expansion, with a series of new members such as $ZrTe_2$ [9], ReS_2 [10], and $PtSe_2$ [11] being added to the family. The number of publications concerning TMD materials in Web of Science has rapidly increased from 63 articles in 2013 to 682 articles in 2023, showing a considerably growing interest. These TMDs with different transition metal centers, covering semiconductor, semimetallic and metallic materials, possess many advantageous physical and chemical properties for electrochemical applications [12], including quantum confinement, tunable bandgap, interlayer coupling, surface effects, and unprecedented large surface area. Specifically, compared to the metal-based materials commonly used in fuel cells, TMDs exhibit more attractive physicochemical properties. The 2D structures with thicknesses as low as a few nanometers and sizes ranging from a few nanometers to hundreds of nanometers, provide a larger specific surface areas for ion absorption and faster surface redox reactions [13]. Moreover, charge distribution occurs between diverse monomers, and synergistic effect can be awakened in structures assembled from TMD materials [14,15]. These exceptional properties of TMDs may lead to superior electrochemical performance in fuel cell technology.

Although TMDs are being continuously refreshed and their physical properties are diversified, materials with fixed properties might not meet the demands of multifunctional applications. Energy applications require the further design of materials into more sophisticated tailored structures [16]. Similar to graphene, the unique 2D structure and immense specific surface area of 2D TMDs also pose challenges in material stacking, which may lead to undesired deterioration of material properties, random structural distortion and heterogeneous interlayer interference [17]. To overcome these critical shortcomings, researchers have opted to customize TMD nanosheets into nanoribbons, nano-flowers, various porous structures, or assemble them into thin-film structures. Controlling the assembly of TMDs into customized nanostructures also presents a series of new physicochemical properties such as strain effects, synergistic effects, and interlayer coupling [18], making TMDs the ideal candidate to replace precious metal materials for electrochemical applications. For example, Qinbai Yun et al. [19] argued in their review that the micro-hollow structures suppress the restacking of 2D TMD thin films. Hollow structures such as MoS_2 microboxes [20], MoS_2 tubular structures [21], and MoS_2/C microspheres [22] have large surface areas and high porosity, allowing for a significant number of accessible active sites to increase the energy density of LIBs. According to Sikandar Aftab et al. [23], 1D heterogeneous devices exhibit better optoelectronic performance compared to 2D nanosheets. For instance, the electrochemical reaction rate of scroll-like structures formed by monolayer WS_2 and MoS_2 is improved by an order of magnitude compared to planar heterostructures [24]. The strain and well-contacted interlayer interfaces synergistically improve the band structure of nanoscroll. Additionally, Juan Su et al. [25] summarized that 2D/2D heterostructures with good face-to-face contact are believed to enhance heterojunction effects due to their larger interface area. As a result, nano-assembly techniques, including chemical vapor deposition (CVD) [26], Langmuir-Blodgett (LB) [27], and template methods [20], are employed to construct these custom nanostructures. These technologies effectively and non-destructively assemble TMDs, enabling the full exploitation of their superior electrochemical properties in applications such as fuel cells.

So far, researchers have summarized the assembly techniques of TMDs in different dimensions and their superior performance in areas such as sensors, optoelectronic devices, electrocatalysis, and gas separation (Table 1). However, there is still a lack of review articles on the application of multi-dimensional TMDs in various modules of fuel cells. In this review, we first overview the promising features of 2D TMDs in terms of programmable electronic, mechanical properties, as well as the effects of complex external environments on materials. In addition, the assembly methods and performance enhancement of multi-dimensional tailored nanostructures of TMDs are demonstrated. These structures include 1D tubes, 2D films and 3D stereostructures. Finally, the application of these tailored nanostructures in catalyst and diaphragm components of fuel cells are examined and compared.

2. The physical properties and appealing characteristics of TMDs during assembly

2D materials, characterized by layered materials with strong intra-layer bonding and weak inter-layer interactions, have gained significant attention in recent years. TMDs are seen as candidates with comparable potential to graphene in several application domains due to their diverse programmable structures. TMDs consist of 39 distinct types differing in chalcogen elements and transition metal centers, which are further divided into 55 polymorphs based on their unit cell and symmetries [18]. These materials exhibit distinct band structures and properties owing to their distinct atomic arrangements. As the research into the modulation of TMDs deepens, establishing the relationship between its lattice constant,

Table 1
Summary of some representative reviews on different dimensions of TMDs and their applications.

Dimension	Application	Year	Ref.
1D	Electronic and optoelectronic devices	2023	[23]
	Energy storage, electronic devices, and sensors	2016	[28]
2D	Catalysis	2019	[25]
	Water desalination and fuel cell	2023	[29]
	Energy conversion and magnetic quantum devices	2023	[30]
	Electronic devices	2017	[31]
3D	Batteries, supercapacitors, and electrocatalytic hydrogen evolution	2018	[19]
	Energy, sensing, and environment	2019	[32]
0D, 1D, 2D	Sensors	2016	[33]
0D, 1D, 2D	Alkali metal ions batteries	2023	[34]
0D, 1D, 2D, 3D	Photocatalytic hydrogen evolution	2022	[35]
0D, 1D, 2D	Biomedicine	2018	[36]
0D, 2D, 3D	Electrochemistry	2021	[37]

electronic structure, and physical and chemical properties has become a crucial step in the assembly of customized nanostructures of TMD (Fig. 1).

The atom-thin 2D materials embodies the physical-theoretical limit of miniaturization. By imposing nanoscale modulation, its electronic properties can be altered to surpass the limitations of macroscopic bulk materials. Their electron structures, namely the band structures, which is closely related to the symmetry and charge density distribution of materials, are the most effective properties of TMDs. The transformed band structures of TMDs can effectively tune the electrical properties by altering the charge distribution and orbital occupation of TMDs. The modified band structure can be achieved through surface modulation methods such as doping, defects, and modification. For instance, Jing Peng et al. [45] manipulated the superconductivity of TaS_2 through the introduction of defects. In metallic TaS_2, the appropriate introduction of Ta atomic defects increased the hole density and enhances the electron-phonon interaction, thereby enlarged the density of state at the Fermi level, which contributed to the critical temperature (T_c) enhancement of superconductivity. Similar effects in atomically doped TMDs are induced by electron donors and acceptors. Lili Zhang et al. [46] doped vanadium atoms onto the Mo sites of the MoS_2 lattice. Considerable gap states were introduced near the valence band, which increased the activity of the S-$3p_z$ orbital and pushed more S-$3p_z$ states to move to the band edge. The significantly enhanced S-$3p_z$ orbital coupling between adjacent layers gave rise to drastically improved conductivity. M. Kamitani et al. [47] utilized intercalation surface modification to alter the electron-phonon coupling in $IrTe_2$. A small amount of Cu intercalation greatly improved the interlayer electron-phonon coupling of $IrTe_2$. It suppressed the structural phase transition from a high-temperature trigonal to a low-temperature monoclinic phase, thus inducing superconductivity.

The improvement of band structure can also be achieved by means of interface control such as heterostructure and layer number control. Heterostructures of emerging metallic or semimetallic TMDs with conventional Mo-and W-based TMDs are capable of improving electronic properties and addressing Fermi-level pinning through programmable band alignment. For example, Hyeokshin Kwon et al. [48] constructed a lateral MoS_2—NbS_2 heterostructure and found that the conduction and valence band edges gradually merged in the interface transition region, and the typical Schottky barrier at edge contacts was absent inside the conduction band. Jing Zhang et al. [49], on the other hand, chose to construct a vertical MoS_2-WS_2 heterostructure. Under interlayer coupling and charge transfer between MoS_2 and WS_2, the vertical epitaxial MoS_2/WS_2 heterostructure demonstrated much lower binding energy of interlayer exciton than the

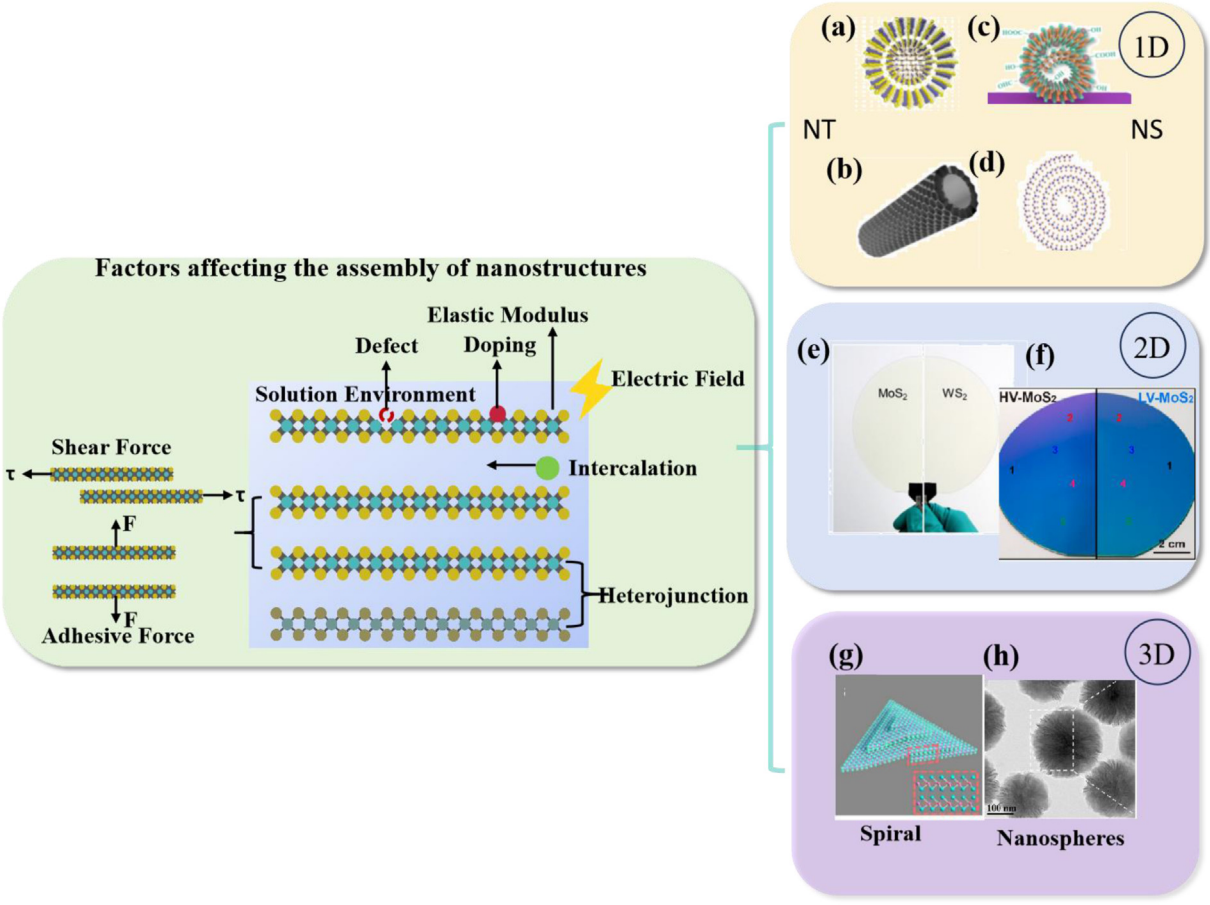

Fig. 1. Assembly of TMDs nanostructures with different dimensions and its influencing factors. (**a**—**d**) 1D tubular structure of TMDs. (a) Reproduced from the study by An et al. [38] with permission from Springer Nature. (b) Reproduced from the study by Zhuo et al. [39] with permission from John Wiley and Sons. (c) Reproduced from the study by Zhang et al. [40] with permission from Elsevier. (d) Reproduced from the study by Zhao et al. [41] with permission from the American Chemical Society. (**e**—**f**) 2D thin film structure of TMDs. (e) Reproduced from the study by Seol et al. [26] with permission from the John Wiley and Sons. (f) Reproduced from the study by Lee et al. [42] with permission from the American Chemical Society. (**g**—**h**) 3D nanostructured architecture of TMDs. (g) Reproduced from the study by Tong et al. [43] with permission from the John Wiley and Sons. (h) Reproduced from the study by Zhang et al. [44] with permission from the American Chemical Society.

monolayer MoS_2 and WS_2. In short, the tunable electrical properties of TMDs are typically interpreted as variations in energy bands near the Fermi levels and in electron-phonon coupling.

In terms of mechanical properties, 2D TMDs exhibit a unique combination of high in-plane elastic modulus and low out-of-plane elastic modulus. As for TMDs, the in-plane elastic modulus among distinct crystal phases of the same material is relatively similar, while it is associated with the thickness and chalcogen elements. For instance, Simone Bertolazzi et al. [50] reported that the in-plane elastic moduli of monolayer and bilayer MoS_2 were 270 ± 100 GPa and 200 ± 60 GPa, respectively, but higher values of 330 ± 70 GPa was reported by Andres Castellanos-Gomez et al. [51] for multilayer (5–25 layers). Transition metal sulfides generally possess the highest elastic modulus, whereas tellurides are known to be the softest. Yufei Sun et al. [52] investigated the in-plane elastic moduli of three phases of $MoTe_2$, and the measured results were all around 100 GPa, only one-third of that observed in MoS_2. In contrast to the in-plane elastic modulus primarily governed by robust covalent bonds, the out-of-plane elastic modulus dominated by van der Waals (vdW) forces is much weaker. Yanyuan Zhao et al. [53] reported that the out-of-plane modulus of MoS_2 and WSe_2 were merely 52.0 and 52.1 GPa, respectively. This disparity between in-plane and out-of-plane mechanical properties enables 2D materials to engage in a myriad of folding and assembly like origami at the nanoscale, simultaneously maintaining high intrinsic strength [54].

The in-plane and out-of-plane elastic modulus are intrinsic properties of materials. Meanwhile, it is also necessary to take note of the complex solid-solid interfaces in 2D assembly structures. The atomically smooth surfaces and weak vdW interactions of 2D materials contribute to low interfacial shear strength [55]. Within TMDs, the interplay between energy barriers and lattice constant can explain this shear stress. Mohammad R. Vazirisereshk et al. [56] suggested that the larger lattice spacing of selenides and tellurides led to a reduction in frictional force in Mo-based TMDs. In TMD heterostructures, the interfacial shear modulus and the interaction between 2D layers and substrates are two critical parameters determining the friction behavior [57]. For example, Mengzhou Liao et al. [58] proposed that the incommensurate contact at the interface gave rise to friction in the MoS_2/graphite and MoS_2/hBN heterostructures. Hongzhi Du et al. [59] and Jaehyung Yu et al. [60] quantitatively characterized the interfacial shear strength of MoS_2 on PET and PDMS as 0.34 MPa and 7.7 ± 2.5 MPa, respectively. The actual application definitely demands stronger interlayer forces between 2D layers for load transfer, so it is crucial to adjust interfacial shear forces during the assembly of tailored nanostructures of 2D materials.

Aside from shear forces, adhesive properties are also taken into account at the solid-solid interface of 2D assembly structures. Distinguishable from shear forces, adhesion energy defines the energy required to separate a 2D material from a surface in the vertical direction. Although vdW interaction is taken for the main force at these interfaces, the measured adhesion energies between TMDs and different surfaces are not the same. Taking MoS_2 as an example, Daniel A. Sanchez et al. [61] measured the adhesion energy of the graphene-MoS_2 interface using the bubble method, which was found to be approximately 140 mJ/m^2. In contrast, Hossein Rokni et al. [62] obtained a measurement of around 269 mJ/m^2 using the indentation method. Even results with the most commonly used SiO_2/Si substrate leap several orders of magnitude [61,63,64]. The complex of interfacial adhesion energy measurement of 2D materials puts forward new requirements for experimental environment and test standards. It is worth noting that the adhesion energy between graphene or MoS_2 and the metal is notably high. Jorge Torres et al. [64] reported that the adhesion energies between MoS_2 and Au substrates and Pt substrates were 1207 and 691 mJ/m^2, respectively. Although fair comparisons between testing results prove challenging, these adhesion data may still provide valuable references for assembling of 2D materials.

To systematically understand the interfaces of assembled structures in 2D materials, it is necessary not only to analyze the internal interaction of the structure in detail, but also to figure out the complex external environment such as solution and applied electric field. In practical conditions, water is an unavoidable factor that could unexpectedly alter the surface chemical properties of 2D materials. For example, Taib Arif et al. [65] found that MoS_2 maintained a relatively smooth state regardless of humidity. However, oxidation occurring at the edges or basal surface defects heightened the sensitivity to water and significantly promoted the average friction because of the stronger localization of surface charges caused by the more electronegative oxygen. Here, water behaved as adsorption rather than intercalation. Taib Arif et al. [66] also discovered that GO exhibited an increasing trend in frictional force with the increase of relative humidity compared to MoS_2. Water molecules were easily intercalated between the GO layers, resulting in a 100% increase in the film thickness and inducing higher roughness. This apparent contrast results from the different hydrophilic and hydrophobic properties of GO and MoS_2 surface.

Moreover, the external electric field may affect phonon vibration, electron motion or electrostatic force [67]. Haojie Lang et al. [68] found that applying a negatively biased voltage brought about the enhancement of nano-friction of functionalized graphene. By adjusting the AFM tip voltage, the friction force was increased by more than eight times owing to the meniscus force of the increased voltage and the electrostatic force induced by the polarization of graphene. In TMD, Bin Shi et al. [69] reported that the negative electric field was apt to lower the friction of the monolayer MoS_2 to the ultra-low friction state. The shift and accumulation of charges between MoS_2 and SiO_2/Si substrates results in electronic tight-binding with high interfacial bonding strength. This suppresses atomic-scale deformation and limits local pinning capabilities, which reduces MoS_2 friction on the substrate by nearly five times.

The programmable electrical properties and unique 2D structure of TMDs offer great flexibility during assembly. However, the large specific surface area and high surface energy of 2D materials contribute to the complexity of adsorption on their surfaces, posing important challenges for tailoring of 2D materials structures for practical applications. Therefore, when assembling 2D material custom structures for practical work, researchers need to consider the material's intrinsic properties and the impact of complex working environments on its mechanical properties. Only through a comprehensive analysis of electrical properties, chemical properties, and mechanical properties such as adhesion and shear forces, can tailored nanostructures of TMD materials be truly cater to the demands of distinct operational conditions.

3. Assembly of TMD-tailored nanostructures

Based on the flexibility of 2D TMDs described above, nanostructures of different dimensions have been successfully assembled to allow for cutting and optimizing the large in-plane shapes and diverse layer-stacking numbers of TMDs at the interface scale. Herein, we outline multiple mechanisms of constructing tailored nanostructures for TMDs, including direct growth, surface tension

assembly and LB assembly, among others. These approaches facilitate the construction of nanostructures in dimensions such as 1D, 2D, and 3D.

3.1. One-dimensional tubes

The conversion of thin films into nanoscale curled structures is an intriguing topic in nanoscience and nanotechnology. It has been observed that 2D TMD sheets, serving as a complement to gapless graphene, can form various 1D structures including nanotubes (NTs) and nanoscrolls (NSs) through simple folding or rolling processes. These curled structures exhibit properties distinct from their film counterparts, significantly impacting properties such as the photovoltaic effect [70], superconductivity [71], flexibility [72] and so on.

As early as 1992, TMD NTs were first discovered by Tenne group [73]. The research focused on the sulfidation of the respective metal oxides as self-sacrificing precursor crystals to develop scalable synthesis processes for NTs. It is currently possible to fabricate well-defined wall, bamboo-like, and nanosheet-based forms [74]. However, research progress on TMD NTs has been almost stagnant as a result of the lack of a simple and efficient growth method for producing structurally defined NTs, unlike CNTs discovered during the same period. Recently, Qinwei An et al. [38] used gold nanoparticles (NPs) as catalysts to directly grow WS_2 NTs with controllable chirality by CVD (Fig. 2a and b). The Au NPs catalyst was observed to provide a unique accommodation site for the reactions of WO_3 vapor, hydrogen, and sulfur. WS_2 shells were then formed on the surface of the NPs, providing seeds for the growth of WS_2 NTs. The yield of WS_2 NTs with a single chiral angle reached ~79% in the optimal growth temperature range. Sifei Zhuo et al. [75] developed hierarchical nanosheets-based MoS_2 NTs with an inner diameter of ~200 nm and thickness less than 10 nm, containing large pores of ~200 nm, and mesopores of ~30 nm, through an anion-exchange reaction. The O^{2-} anions of the inorganic-organic hybrid precursor MoO_3-EDA nanowires (NWs) slowly exchanged with S^{2-} to form 2H–MoS_2 (Fig. 2c and d). The dissolution of ethylenediamine (EDA) in the solvent and the outward diffusion of MoO_3-EDA were crucial in the formation of MoS_2 NTs. This highly exposed porous structure shows high photocurrent density in combination with low-cost starting materials. M. Remškar et al. [76] used $Mo_6S_2I_8$ NWs as precursors to successfully encapsulate MoS_2 fullerenes in MoS_2 NTs through vulcanation (Fig. 2e). The synthesized nanopods had a wall thickness of ~13 nm and a length of 1 μm, and the size of the inner encapsulated fullerenes varied from 40 nm to 285 nm (Fig. 2f). The internal NWs decomposed after the iodine was completely removed and released, resulting in the sulfation and diffusion of the remaining internal material to form MoS_2 fullerenes.

Besides the morphology of NTs, 1D NSs derived from 2D nanosheets rolling in a coaxial manner are also of great interest in the fields of catalysis, energy storage and optoelectronics. This is attributed to their spiral tubular structure, open ends, and tunable interlayer distance. So far, a variety of methods have been employed to prepare TMD NSs, including argon plasma assisted scrolling [77], supercritical fluid assisted scrolling [78], amphiphilic organic

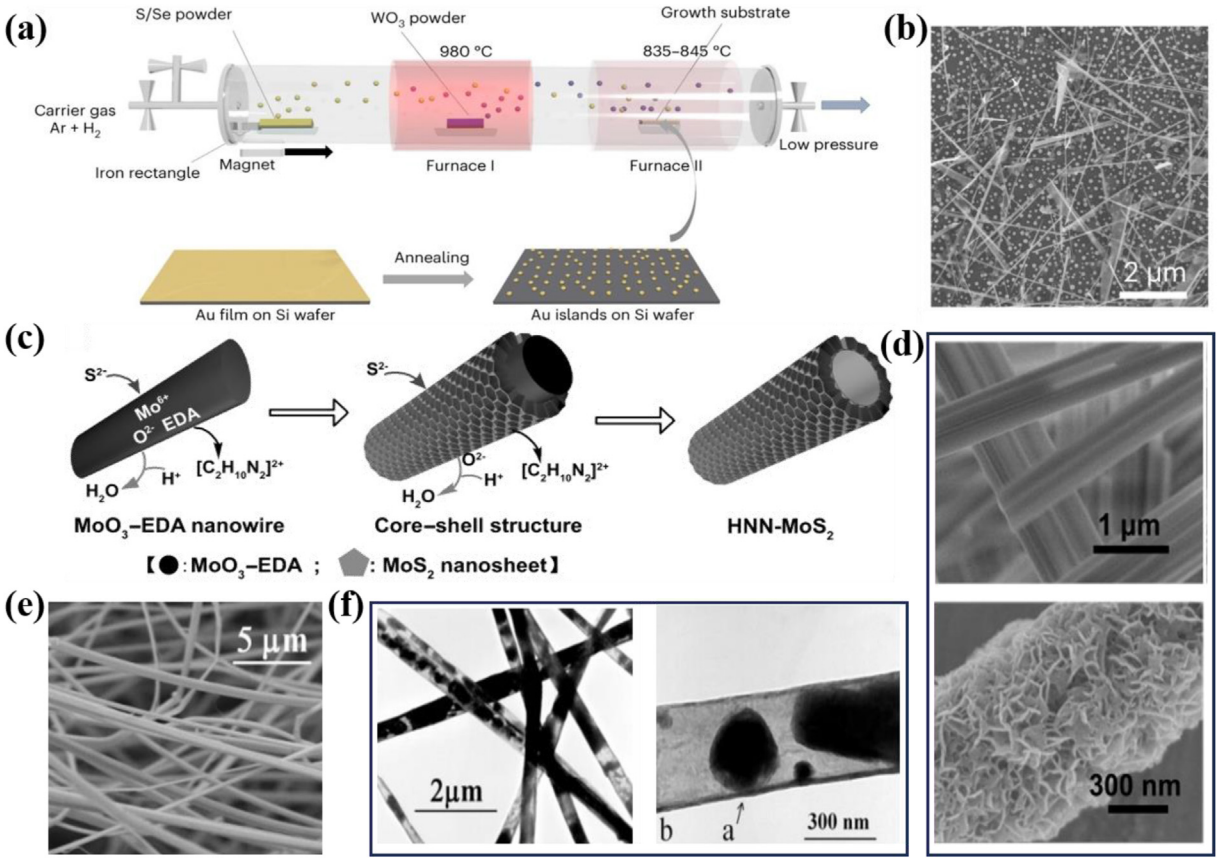

Fig. 2. Formation mechanism and characterization of TMD NTs. (**a**) Schematic illustration showing the preparation of the Au NP catalysts and the CVD growth of TMD NTs. (**b**) SEM of the WS_2 NTs grown at 835–840 °C. (a–b) Reproduced from the study by An et al. [38] with permission from Springer Nature. (**c**) Schematic representation of the synthesis of hierarchical nanosheet-based MoS_2 NTs. (**d**) SEM images of solid hybrid nanowires and hierarchical nanosheet-based MoS_2 NTs. (c–d) Reproduced from the study by Zhou et al. [39] with permission from John Wiley and Sons. (**e**) SEM of the $Mo_6S_2I_8$ precursor crystals. (**f**) TEM images of the MoS_2 NTs with encapsulated MoS_2 fullerene-like nanoparticles. (e–f) Reproduced from the study by Remškar et al. [76] with permission from John Wiley and Sons.

molecule assisted scrolling [79], volatile organic solvent-assisted scrolling [80], and alkaline drop assisted scrolling [81]. Among them, organic solvents and alkaline droplets are commonly used as assisting agents. Lu Zhang et al. [40] fabricated carbon/oxygen functionalized InSe NSs through two steps: 1) electrochemical intercalation to synthesize nanosheets, and 2) organic solvent-assisted scrolling (Fig. 3a). Specifically, CTAB-InSe nanosheet suspension was spin-coated onto interdigital electrode surface, followed by solvent evaporation and rolling under vacuum at 80 °C, to prepare NSs with a hollow tubular structure of 1–5 μm in diameter and about tens of micrometers in length (Fig. 3b and c). The rolling process was driven by Marangoni forces: during the solvent evaporation, a temperature gradient was generated between the liquid-vapor interface along the vertices and edges, leading to a surface tension gradient. This surface tension gradient induced fluid flow and rolled up the edges of the nanosheets. However, this fabrication method inevitably leaves residual organic solvents or alkaline impurities in the NSs, which severely affects the interlayer distance

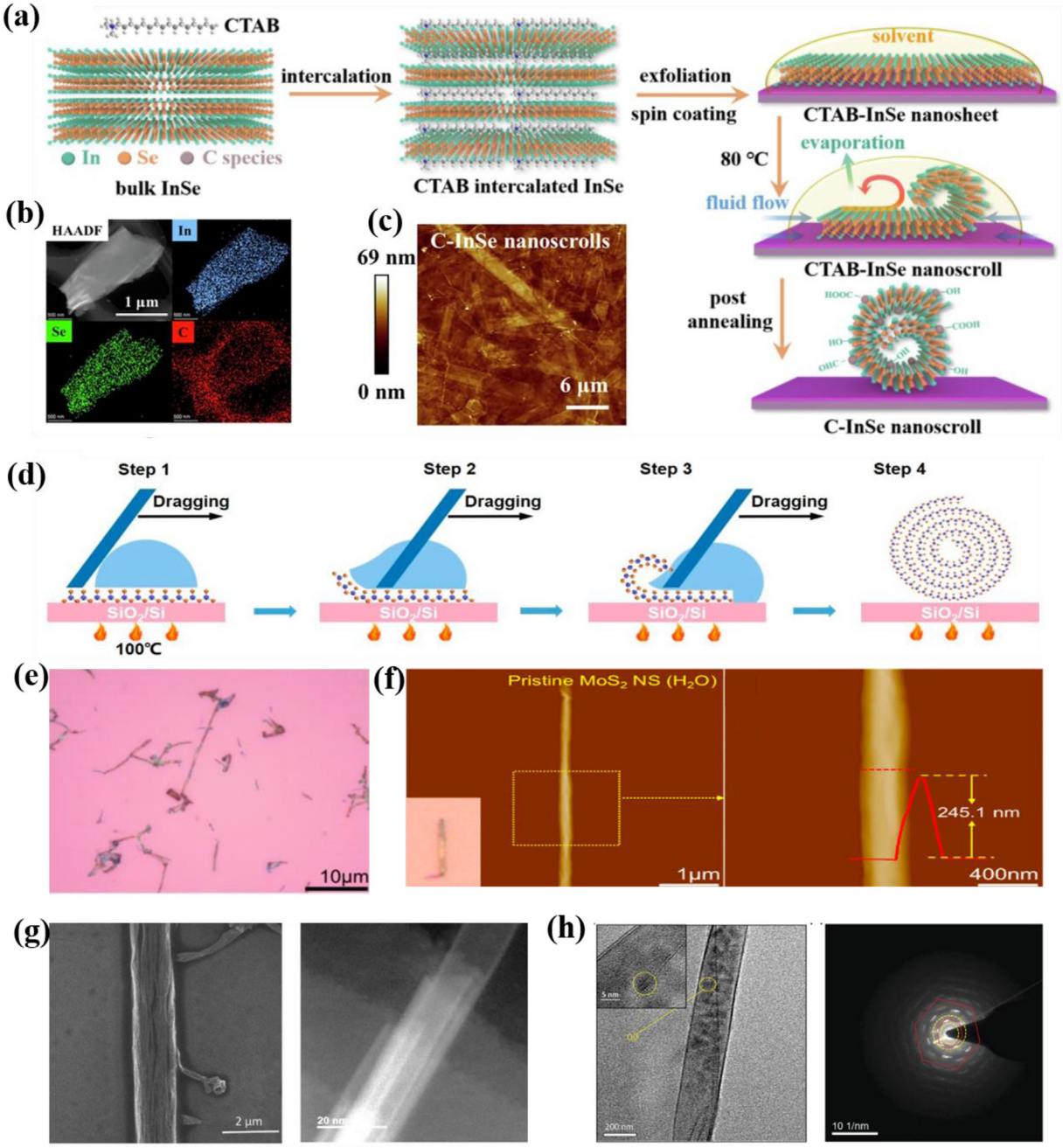

Fig. 3. Formation mechanism and characterization of TMD NSs. (**a**) Schematic diagram of the process of C–InSe NS preparation. (**b**) High angle annular dark field (HAADF) image and corresponding EDS mapping of one C–InSe nanosheet. (**c**) AFM of C–InSe NSs. (a–c) Reproduced from the study by Zhang et al. [40] with permission from Elsevier. (**d**) Illustration of the Formation of the MoS_2 NS. (**e**) OM image and (**f**) AFM of MoS_2 NS prepared by dragging water droplet at temperature of 100 °C. (d–f) Reproduced from the study by Zhao et al. [41] with permission from the American Chemical Society. (g) SEM and HAADF-STEM images of a single heterojunction-NS. Reproduced from the study by Ghosh et al. [24] with permission from the American Chemical Society. (**h**) HRTEM image of WS_2 NS hybridized with CdSe–ZnS core-shell QDs and the corresponding SAED pattern of an individual hybridized WS_2 NS. Reproduced from the study by Ghosh et al. [87] with permission from the John Wiley and Sons.

and optoelectronic properties of TMD NSs [82]. Ying Zhao et al. [41] designed an organic solvent-free method, which resulted in MoS_2 NSs with enhanced interlayer coupling and improved photosensitivity. Monolayer MoS_2 or WS_2 nanosheets grown by CVD on SiO_2/Si substrate were heated on a 100 °C hotplate for 10 min, and then deionized water droplets were dragged with a coverslip at a certain speed (Fig. 3d). During this process, MoS_2 nanosheets were rolled up as the water droplet moved, forming NSs with heights ranging from tens to hundreds of nanometers and lengths of tens of micrometers (Fig. 3e and f).

Actually, the 1D structures of various TMDs including MoS_2 [83], $MoSe_2$ [84], and WSe_2 [85] have been extensively studied. And new structures have been proposed, including different 1D vdW heterostructures and 1D core-shell structures. These 1D structures exhibit attractive properties on electronic and optoelectronic devices. Rapti Ghosh et al. [24] rolled the heterostructure arranged by MoS_2 and WS_2 into NS through evaporation-assisted assembly (Fig. 3g). The heterojunction-NS overcomes the inherent drawback of low electrochemical reactivity of 2D TMDs, resulting in an evident rise in exchange current density to 1.44×10^{-4} A/cm^2 and a decrease in Tafel slope to 39 mV/dec. The performance is comparable to that of noble metal catalyst systems in the photoelectrochemical hydrogen evolution reaction process. In detail, atomically accurate heterojunctions benefit the carrier separation process, and the local strain generation and the layered wrapping structure of the NSs facilitate the electron transfer process. The synergy enables efficient charge carrier injection from the semiconductor surface to protonic sites in the electrolyte solution, leading to an enhancement in the electrochemical reaction rate of heterojunction-NS. Such precise structural control clearly holds remarkable value for catalyst design in the energy field.

Apart from these relatively simple heterostructures, Bei Zhao et al. [86] reported a more complex scroll structure of vdW heterostructures, and extended to 2D/2D/2D vdW superlattices, as well as materials beyond 2D, including 3D thin films and 1D NWs, to generate mixed-dimensional vdW superlattices such as 3D/2D, 3D/2D/2D, 1D/2D and 1D/3D/2D vdW superlattices. This study employed multiple fabrication methods, including CVD and atomic layer deposition. Notably, electrical transport studies revealed that superlattice formation modulates the electronic band structure and dimension, giving rise to a transition of the transport characteristics from semiconductive to metallic, with greatly increased conductance. As researchers extensively explore higher-dimensional materials, lower-dimensional 0D quantum dots (QDs) have captured attention. Fig. 3h illustrates the 0D/2D structure created by the hybridization of colloidal QDs and NSs. Rapti Ghosh et al. [87] used CdSe−ZnS core-shell QDs solution to spin coat a single layer of WS_2 on SiO_2/Si substrate, and then dropped acetone onto it. The capillary force of evaporation of the organic solvent helped the hybrid nanosheets to curl into mixed NSs.

Numerous studies have demonstrated the successful development of tailored 1D nanostructures in the form of heterostructures and core-shell structures, which can unleash the electrical and electrochemical potential of TMD materials and overcome the low conductivity and low electrochemical reactivity caused by the semiconductor bandgap. Although sophisticated 1D tailored nanostructures have been achieved, further research is required to realize the practical application of TMD-based 1D nanostructures in the energy field. In this regard, while the synthesis of various TMD NTs and NSs has been reported, high-yield synthesis has been particularly well-established for WS_2 NTs [88]. It is crucial to develop a universal method for large-scale synthesis. Only on this basis, further assembly of TMD 1D tailored nanostructures into network films and composites can be put into research and practical production.

3.2. Two-dimensional films

Owing to the strong interlayer coupling of 2D nanosheets, there is a clear trend for face-to-face stacking rather than edge-to-edge geometry [89]. Indubitably, such face-to-face stacked material with lower surface area will greatly reduce the active functional area. Assembling 2D TMD nanosheets into high-quality customized 2D thin films with more active exposed regions holds great importance for material properties in the energy field. The current reports can be divided into two directions: direct growth of ordered structures and assembly after monomer synthesis.

Direct growth methods mainly include physical vapor deposition (such as vacuum evaporation [90], magnetron sputtering [91], pulsed laser deposition (PLD) [92], etc.) and CVD [93]. These methods have matured in preparing single-layer and double-layer centimeter-scale TMD films, including MoS_2, WS_2, $MoSe_2$, WSe_2, and others, and the precursors have also evolved from metal oxides to liquid precursors and metal organics. Metal-organic chemical vapor deposition (MOCVD) uses metal organics to replace traditional solid sources such as molybdenum oxide, and its sulfur source is typically sulfur-containing gases. Minsu Seol et al. [26] selected $Mo(CO)_6$, $W(CO)_6$, and $(C_2H_5)_2S_2$ as precursors for Mo, W, and S respectively, to obtain 6-inch wafer level monolayer MoS_2 and WS_2 films (Fig. 4a and b). Moreover, using a thermal release tape, the grown TMD could successfully transfer the film from the SiO_2/Si substrate to the desired substrate. Since the precursors participate in the reaction process in the form of gas, it could be rolled to the high-throughput growth of diverse TMDs, both semiconductor (for example $MoSe_2$ or WTe_2) and metal (for example $NbSe_2$ or TaS_2) [94], while ensuring excellent spatial homogeneity and high quality with well-stitched grain boundaries. Yet Junghyun Lee et al. [42] chose to combine the Mo source and sulfur source into one to synthesize vacancy-tunable wafer-scale through 1) liquid-phase ligand exchange reaction to form $Mo(TDT)_x$ (tert-dodecylmercaptan) solution, and 2) stepwise thermal annealing process. By controlling the relative molar ratio of TDT and $MoCl_5$ in the initial precursors, it is easy to adjust the sulfur vacancy concentration in the MoS_2 film, which increases the charge transfer through the partial doping effect. Likewise, it can be used to synthesize $MoSe_2$, WS_2, and WSe_2 films.

Nevertheless, given the energy consumption and the harsh preparation conditions, such as CVD requiring high temperatures, vacuum, and non-flexible substrate, it is far more likely that the synthesis of monomers followed by assembly had greater universality and possibility for large-scale practical application. There are roughly three types of monomer synthesis strategies that facilitate subsequent assembly: mechanical exfoliation [95], liquid phase exfoliation [96], and chemical synthesis [97]. Liangzhu Zhang et al. [98] studied a general solid phase exfoliation (SPE) strategy by ball milling for the fabrication of 18 types of MX_2 (M = Mo, W, V, Nb, Ta, Ti, X = Te, Se, S) nanosheets from corresponding crack-induced bulk crystals (C-MX_2) (Fig. 4c). The exfoliated nanosheets (Fig. 4d and e) could be stored in powder form or easily dispersed in water with ideal concentration for follow-up thin film and device fabrication. The fabricated $MoSe_2$ micro-supercapacitors display ultra-high electrochemical response, ascribed to the abundance of 2D channels between $MoSe_2$ layers for rapid electrolyte ion insertion and charge transfer. Liquid-phase exfoliation enables low-cost production of a large quantity of TMD nanosheets, such as ReS_2 nanosheets [99]. But the dispersed concentration of TMDs obtained is relatively low, and the organic solvents used to stabilize 2D nanosheets (such as polyvinylpyrrolidone, and N-methyl pyrrolidone) are usually toxic. Anupam Giri et al. [100] synthesized TMD nanosheets (MoS_2, WS_2, $MoSe_2$, WSe_2, etc.) by microwave-assisted chemical synthesis. The number of layers of the nanosheets could

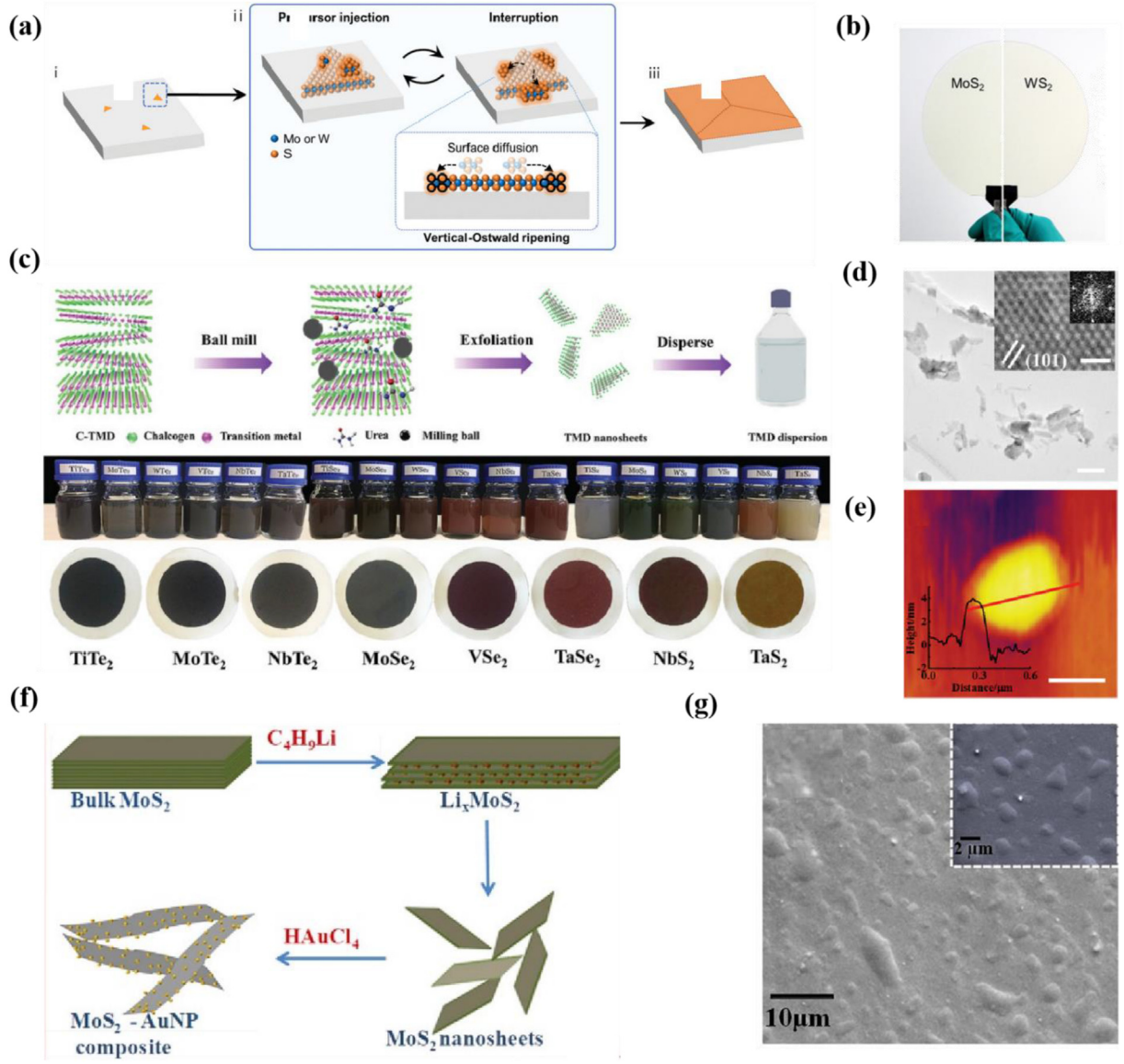

Fig. 4. Assembling 2D TMD nanosheets into 2D thin films. (**a**) Schematic of the growth mechanism by pulsed MOCVD. After nucleation in the early stage (i), lateral growth is induced by repeating the precursor injection and interruption steps (ii), which results in continuous monolayer TMDs (iii). (**b**) Photograph of wafer-scale monolayer MoS_2 and WS_2. (a–b) Reproduced from the study by Seol et al. [26] with permission from the John Wiley and Sons. (**c**) Schematic illustration of solid-state exfoliation of TMD nanosheets by ball milling from the C-TMD materials. (**d**) Low magnification TEM of $MoSe_2$ nanosheets, scale bar 200 nm. Insets are the corresponding HRTEM and FFT images, scale bar 1 nm. (**e**) AFM of $MoSe_2$, scale bar 50 nm. (c–e) Reproduced from the study by Zhang et al. [98] with permission from the John Wiley and Sons. (**f**) Schematic of the synthesis of MoS_2 nanosheets and their decoration by gold NPs. (**g**) SEM images of MoS_2–AuNP/ITO electrode. (f–g) Reproduced from the study by Solanki et al. [106] with permission from the American Chemical Society.

be precisely controlled by varying the concentrations of $MoCl_5$/WCl_4 and thiourea/selenourea in the electrolyte. The downside to this option is that most of the synthesized nanomaterials are particles with complex structures.

After the monomer is synthesized using the above method, the assembly strategy is another crucial factor in determining whether the thin films are suitable for practical production. Numerous conventional and advanced methods have been introduced into the production of TMD films, including:1) spin coating [101], spray coating [102], dip coating [103], 2) drop casting [104], 3) vacuum filtration [105], 4) LB technique [106], 5) printing, etc. Wherein, the assembly methods such as spin coating, dip coating, drop casting and vacuum filtration assemble the film on the substrate using centrifugal force, evaporation force, pressure and other external forces. These methods provide a fast and economical preparation method for 2D films, but the disadvantages are the limitations of small-area coatings and the lack of nanoscale control of film thickness. LB film deposition is an interface-induced self-assembly method performed at the air-liquid interface. It allows for the manipulation of materials at the molecular level. And it has been regarded as an effective method for the controlled preparation of molecular layer thin films on various substrates. Shipra Solanki et al. [106] reported the LB film assembly of MoS_2 composites (Fig. 4f). The MoS_2–AuNP composite was dispersed in chloroform ($CHCl_3$) and the solution was then spread onto the water subphase and left to evaporate $CHCl_3$. At an optimized target pressure of ~12 mN/m, LB monolayers of the MoS_2–AuNP composite have been shaped at the air-water interface (Fig. 4g). The Au NPs not only heightened the charge transfer performance of the composite but also acted as spacers between nanosheets to refrain them from

restacking. In addition, Yefeng Zhang et al. [27] reported a surfactant-free method to deposit chemically exfoliated 1T MoS_2 onto the air-water interface. Through a typical diffusion process, MoS_2 flakes self-assembled spontaneously near the edge of the LB trough to form dense tiled islands. This method does not destroy the films, nor does it leave any residue. Beyond these methods, recently reported techniques such as layer-by-layer assembly [107], printing [108], and electrophoretic deposition [109] have shown great potential for commercial production of 2D films. These methods remain to be explored for TMD-based films.

Ideal thin films for energy applications should be highly crystalline, expose the active region, and be chemically stable and mechanically robust. Thin TMD films with few layers are held together by vdW interaction force, yet, weak intermolecular forces sometimes lead to stability issues causing the films to deform or even fracture. Therefore, it is the key to pay attention to individual nanosheets' quality and the films' encapsulation or composite to ensure the true physical and chemical properties of 2D TMD films.

3.3. Three-dimensional stereostructures

The 3D structure has been proved to be an effective approach to solve the insufficient active surface exposure caused by the restacking of nanomaterials. Typically, these 3D TMD structures possess the following advantages: 1) The active sites of TMD nanosheets can be fully exposed. 2) Abundant holes or channels can effectively shorten the ion transport distance. 3) The pores in 3D TMD framework can effectively buffer the volume expansion during application [19]. So far, a variety of 3D TMD structures such as nanoboxes [20,110,111], nanocages [112,113], nanoflowers [114–121] and hollow nanospheres [44,122–125] have been assembled by researchers using TMD nanosheets. Hydrothermal synthesis [115,116,121], CVD [43,117,126,127] and layer-by-layer stacking [128,129] are standard assembly methods.

Hydrothermal synthesis is the most common method to construct 3D TMD. By adjusting parameters such as reaction temperature, time and precursor amount, researchers synthesized 3D TMD with different morphologies and structures. In addition, by integrating conductive carbon materials with TMD nanosheets, the conductivity of 3D TMD can be further improved [130,131].Templates are often used to obtain microporous structures during the hydrothermal synthesis process. For example, Lei Zhang et al. [20] synthesized MoS_2 microboxes constructed by ultrathin nanosheets. Meanwhile the $MnCO_3$ templates were transformed into MnS microtubules, which pickling could easily remove. As the anode material, the microboxes showed excellent cycling performance. The polarization curve remained basically unchanged after 500 cycles in an acidic environment. The hierarchical MoS_2 microboxes also displayed enhanced lithium storage and hydrogen evolution performance, which was attributed to the sufficient active sites of 3D TMD architecture. Xiaoxia Zuo et al. [112] synthesized the hollow MoS_2 nanocages. The NH_3 generated by the solution reaction was used as the bubble template to construct the hollow structure of the nanocages with abundant active sites. When used as an anode material for LIBs, the hollow structure can provide a large expansible space for the volume change during the cycle. Without templates, hydrothermal synthesis can also produce 3D TMD structures through nanosheet self-assembly. Sanpei Zhang et al. [44] synthesized 3D MoS_2 nanospheres with ultra-thin nanosheets as walls using hydrothermal synthesis (Fig. 5a and b). Due to the high surface energy of MoS_2 nanosheets, PVP additives were tightly absorbed on the planes, which effectively prevented 2D nanosheet re-stacking and drove 2D nanosheets to radially assemble into 3D nanospheres. Recently, Sonam Rani et al. [115] synthesized MoS_2 nanoflowers (Fig. 5c) by one-step hydrothermal synthesis and clarified the formation mechanism of this 3D architecture. The molybdenum and sulfur precursors dissociated to form MoO_3 and H_2S. And then MoO_3 was reduced to MoO_2 by H_2S. Subsequently, the reaction of intermediate and H_2S resulted in the formation of MoS_2 nuclei, which further grew into MoS_2 nanosheets and assembled into nanoflowers [132,133]. This study shows that adjusting the reaction time to control the interlayer spacing in hydrothermal synthesis is an effective method to improve the electrochemical performance of MoS_2 nanoflowers.

Compared to hydrothermal synthesis, CVD and layer-by-layer stacking methods can produce 3D TMD structures with high quality and precise layers. In a CVD process, porous inorganic foams often act as templates because of the inherent porous structure. For example, in a CVD process, Xiumei Geng et al. [126] developed vertical MoS_2 nanosheet arrays using Ni foam templates mediated by graphene. Without the addition of templates, 3D TMD structures can also be prepared by CVD process. Xipeng Tong et al. [43] synthesized spiral pyramid $MoTe_2$ through CVD (Fig. 5d). The spiral pyramid had a large number of HER active sites due to the plentiful edge and edge vacancies. The continuous dislocation lines in the helical structure can be used as a solenoid to carry the screw current, which increased the vertical electronic conductivity. The spiral $MoTe_2$ microcell achieved an ultrahigh current density of 3000 mA/cm^2 with only 0.4V overpotential. Processes such as programmed vacuum stacking and PLD have been used to stack nanosheets layer upon layer to prepare 3D TMD architectures. Kibum Kang et al. [128] prepared high-quality heterogeneous TMD films with centimeter-scale by vertically stacking individual single-layer TMD layer by layer through programmed vacuum stacking process. The initial layer L_0 was peeled off the substrate. And then L_0/TRT was pressed on top of the next layer L_1 in a vacuum chamber. However, this technique requires depositing each TMD individually for stacking, which is a highly repetitive and complex process. Subsequently, Sehun Seo et al. [129] used a simpler in-situ process PLD to stack TMD nanosheets to produce multi-heterogeneous structures of TMDs (Fig. 5e). In this work, adjusting the number of laser pulses can precisely control the number of layers of heterogeneous TMD structures. Vertically stacked MoS_2/WSe_2 and $MoS_2/WS_2/WSe_2$ multi-heterostructure TMDs on centimeter-scale p-Si substrates were successfully prepared.

The electrical properties of 3D TMD structures can be further enhanced by integrating conductive carbon materials. Recently, Nabilah Al-Ansi et al. [134] innovatively incorporated carbon polymer dots (CPDs) in the process of self-assembly of MoS_2 nanosheets to prepare 3D nanoflower-like spheres of MoS_2@CPDs. The MoS_2@CPDs composite had a uniform 3D flowerlike nanosphere structure. With the increase of CPDs content, the interlayer spacing between MoS_2 layers augmented and the aggregation decreased. However, when the amount of CPDs increased to 0.15 and 0.2g, CPDs occupied the interlayer spacing of MoS_2, causing the nanoflower structure to disappear. Meanwhile CPDs can effectively improve the electrochemical performance of MoS_2 by alleviating volume expansion and avoiding layer aggregation. MoS_2@CPDs electrode displayed excellent capabilities of 583.4 mAh/g after 1000 cycles in high density current 5 A/g. Nirul Masurkar et al. [117] used CVD to grow $MoSe_2$ nanoflowers on 3D carbon cloth (CC). This study shows that $MoSe_2$ nanosheets are patterned into nanoflower at 850 °C. $MoSe_2$ nanoflowers are constructed by several layers of nanosheets perpendicular to the substrate, a large number of unsaturated edge active sites are exposed, making them exhibit enhanced electrocatalytic activity.

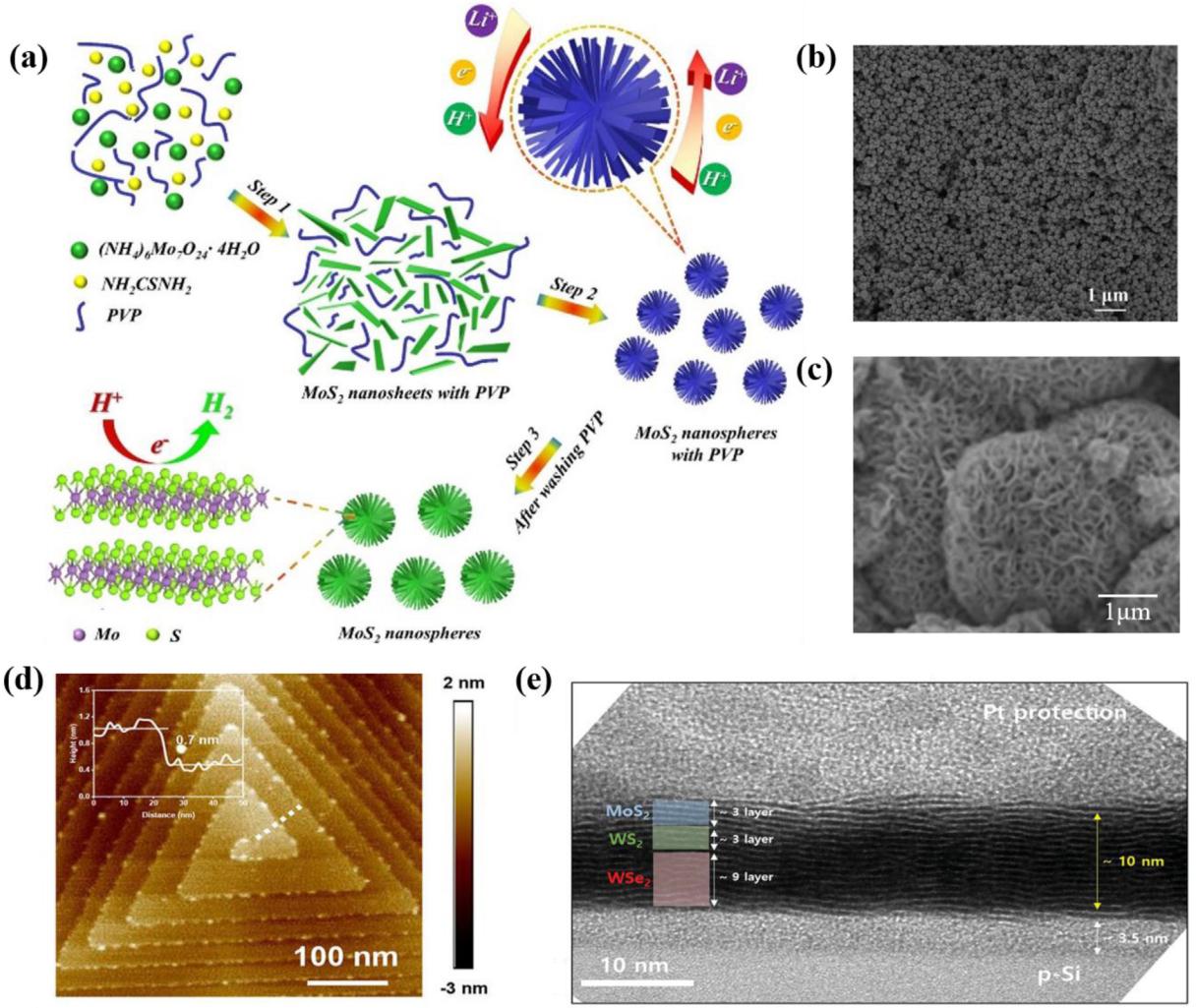

Fig. 5. Preparation mechanism and characterization of 3D TMD stereostructures. (**a**) Schematics depicting the formation of the 3D radially oriented MoS_2 nanospheres. (**b**) Low-magnification FESEM image of the 3D radially oriented MoS_2 nanospheres. (a–b) Reproduced from the study by Zhang et al. [44] with permission from the American Chemical Society. (**c**) FESEM image of MoS_2 nanoflowers synthesized at 220 °C for 50 h. Reproduced from the study by Rani et al. [115] with permission from Elsevier. (**d**) AFM image of spiral $MoTe_2$. Reproduced from the study by Tong et al. [43] with permission from the John Wiley and Sons. (**e**) Cross-sectional HRTEM image for $MoS_2/WS_2/WSe_2$ thin film. Reproduced from the study by Seo et al. [129] with permission from the John Wiley and Sons.

In the process of building 3D TMD architectures, templates are often used to form diverse porous structures. However, selective etching of templates will result in lower crystallinity of the material and defective structures [17]. 3D TMDs prepared without templates have greater degrees of freedom and a greater variety of nanostructures, but they tend to have lower consistency, such as aggregation and uneven size distribution. Generally speaking, these methods have their own advantages and disadvantages and should be chosen based on actual needs.

3.4. Effects of multi-dimensional structures on TMDs

By employing diverse assembly mechanisms, nanostructures with multiple dimensions have been successfully engineered. The assembly of TMDs from 2D structures to rich multi-dimensional structures shows many interesting property changes. These changes cover a range of physical and chemical properties encompassing optics, electricity, and electrochemistry.

1D curled structures exhibit excellent electrical and photoelectrochemical properties. Low conductivity has always been a major factor limiting the application of TMDs in electronic devices, optoelectronic devices, and electrocatalysis. Transforming TMDs from 2D to 1D curled structures allows for material encapsulation layer by layer, effectively promoting electron transfer processes. Bei Zhao et al. [86] fabricated TMD field-effect transistors (FET) on SiO_2/Si substrates to compare the electrical transport characteristics of SnS_2/WSe_2 heterostructures and the scroll structure formed by heterolayers. As shown in Fig. 6a and b, the output characteristics of NSs exhibited high conductivity, with drain current at zero gate voltage being more than 5 orders of magnitude larger than that of the heterostructure. This transition from semiconductor-like features to metallic-like features is closely related to a significant reduction in bandgap and intimate interlayer vdW interactions within the scroll structure. Rapti Ghosh et al. [24] investigated the source of massive charge accumulation in WS_2/MoS_2 heterojunction-NS by photoluminescence spectroscopy. The decrease in photoluminescence intensity of the NS indicated a reduced efficiency of radiative recombination within the heterojunction (Fig. 6c). This could be attributed to two factors: firstly, the tensile strain on the scroll walls leads to a lowering of K-point positions in the valence band (Fig. 6d), resulting in a decrease in optical recombination rate; secondly, adjacent heterojunctions stacked at the scroll walls form an extended superlattice. These changes in band structure not only increase the concentration of photoexcited carriers within the

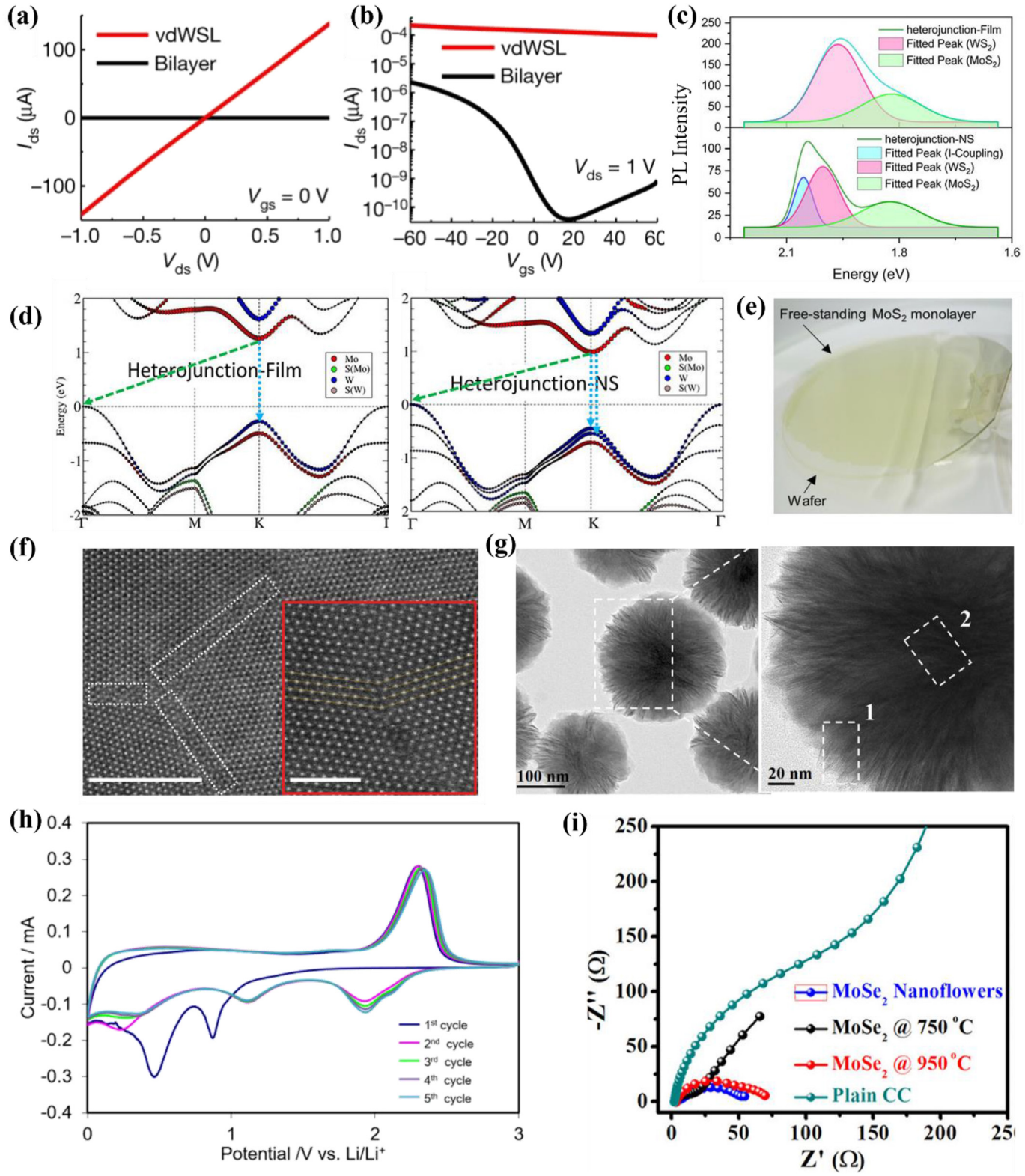

Fig. 6. Effects of multi-dimensional structures on the properties of TMDs. (**a**) Output characteristics of the SnS_2/WSe_2 roll-up FET and the SnS_2/WSe_2 heterobilayer FET at $V_{gs} = 0$ V. (**b**) Transfer characteristics of the SnS_2/WSe_2 roll-up FET and the SnS_2/WSe_2 heterobilayer FET at $V_{ds} = 1$ V. (a–b) Reproduced from the study by Kim et al. [86] with permission from Nature. (**c**) PL spectra of WS_2/MoS_2 heterojunction film and WS_2/MoS_2 heterojunction NS. (d) DFT-calculated band structures for WS_2/MoS_2 heterojunction film and WS_2/MoS_2 heterojunction-NS. (c–d) Reproduced from the study by Ghosh et al. [24] with permission from the American Chemical Society. (**e**) Wafer-scale free-standing MoS_2 film de-bonded from the substrate. (**f**) HAADF-STEM image of MoS_2, showing the grain boundary (white-dotted square region), scale bar 5 nm. Inset is the high-resolution STEM image of the grain boundary, scale bar 5 nm. (e–f) Reproduced from the study by Seol et al. [26] with permission from the John Wiley and Sons. (**g**) TEM and high-magnification TEM images of the 3D radially oriented MoS_2 nanospheres. Reproduced from the study by Zhang et al. [44] with permission from the American Chemical Society. (**h**) CV plots of the MoS_2 electrodes in the voltage range of 0–3 V at a scan rate of 0.2 mV/s. Reproduced from the study by Wang et al. [122] with permission from the John Wiley and Sons. (**i**) EIS Nyquist plot of $MoSe_2$ nanoflowers compared with $MoSe_2$ grown at 750 °C, 950 °C and blank CC. Reproduced from the study by Masurkar et al. [117] with permission from the American Chemical Society.

heterojunction but also enhance electrochemical reaction rates. A significant reduction in charge transfer resistance for heterojunction-NS was observed in electrochemical impedance spectroscopy.

To fabricate large-area 2D films from disordered TMD nanosheets, the primary challenge lies in the issue of stacking, which is a significant concern for TMD materials. In practical applications, it is often desirable to reduce the number of layers in TMD nanosheets. This necessitates overcoming the vdW interaction between TMD layers to achieve high-quality wafer-level films. Minsu Seol et al. [26] directly grew MoS_2 thin films using MOCVD, which existed independently in water and exhibited a continuous and well-sealed structure (Fig. 6e). In the STEM image of Fig. 6f, the film showed a polycrystalline structure without visible pores, with uniform and defect-free grain structures. Furthermore, mass manufactured MoS_2-based FETs were used to evaluate their spatial uniformity. The threshold voltage difference was found to be 0.6 ± 0.1 V in the transfer characteristics curves of 900 randomly selected FET devices, indicating that the electrical performance at the MoS_2/Al_2O_3 interface is also spatially uniform. For the method of assembling thin films after monomer synthesis, it is necessary to investigate the stability of TMD colloidal dispersions. Liangzhu Zhang et al. [98] determined the surface charge of TMDs in colloidal dispersions using zeta potential measurements. The zeta potentials of all TMDs ranged from −37.8 to −21.5 mV. The pronounced surface charge facilitates repulsion between nanosheets, effectively counteracting aggregation induced by vdW forces.

Compared with 1D structures and 2D films, 3D TMD architectures cover the largest variety of custom structures. The nanoboxes, nanoflowers and nanospheres have greatly enriched the TMD topography library. The 3D architecture can preserve the rich active sites and surface area of TMD nanosheets. The study of Sufeng Wei et al. [114] showed that the excellent electrical conductivity and inherent high specific surface area of nanosheets were retained during the process of self-assembly into nanoflowers. Both MoS_2 nanoflowers and nanosheets were composed of 1T and 2H phase MoS_2. The 1T phase MoS_2 in nanoflowers was about 78.0%, which was similar to that of MoS_2 nanosheets (75.3%). The structure of MoS_2 nanosheets in 3D nanospheres in the study of Sanpei Zhang et al. [44] was also well preserved (Fig. 6g). In addition, the hollow structure of 3D TMD can adapt to large volume changes in electrochemical reactions to improve cycle stability. Yawen Wang et al. [122] studied the voltammetry of MoS_2 hollow nanospheres in different cycles and found that cyclic voltammetry (CV) profiles almost overlap (Fig. 6h). The 3D TMD structure is usually built directly on the conductive substrate, and the existence of the conductive backbone network solves the inherent charge transfer problem. Nirul Masurkar et al. [117] synthesized $MoSe_2$ nanosheets directly on CC. Their molecular layer structure was altered and showed a significant increase in electrocatalytic HER activity. Electrochemical impedance spectroscopy illustrated the enhanced charge transfer activity of the $MoSe_2$/CC composite, with nanoflower samples exhibiting a charge transfer resistance of 60 Ω, which is lower than that of $MoSe_2$ grown at 750 °C (125 Ω), 950 °C (90 Ω) and blank CC (150 Ω) (Fig. 6i).

Through various assembly mechanisms and multi-dimensional nanostructure designs, TMDs materials have demonstrated numerous intriguing property changes. These findings hold significant importance for understanding and developing novel nanomaterials. Additionally, the design of multi-dimensional structures has brought new opportunities and challenges to fuel cell technologies.

4. TMDs tailored nanostructures in fuel cells

Fuel cell is considered as one of the most promising sustainable power generation technologies on account of its high efficiency, zero pollution and low noise. Currently, the widely adopted classification method is based on the type of electrolyte. Fuel cells are divided into five main categories: Proton Exchange Membrane Fuel Cells (PEMFC) [135,136], Alkaline Fuel Cells (AFC) [137], Phosphoric Acid Fuel Cells (PAFC) [138], Molten Carbonate Fuel Cells (MCFC) [139], and Solid Oxide Fuel Cells (SOFC) [140] (Fig. 7). These five types of fuel cells primarily use hydrogen as fuel. In addition to these, there are also Direct Alcohol Fuel Cells (DAFC) that directly utilize alcohols as fuels and Microbial Fuel Cells (MFC) [141,142] that employ biomass and microorganisms for power generation.

All fuel cells comprise three fundamental components: the cathode, anode, and electrolyte. On the anode side, fuel undergoes oxidation. The most popular fuels in the market are hydrogen and methanol. Compared to hydrogen, methanol exhibits greater abundance and higher energy density. More importantly, methanol remains in a liquid state at room temperature, thereby significantly reducing transportation and storage costs [143]. Fuel cells using methanol as a fuel may potentially achieve commercialization earlier than hydrogen fuel cells. Specifically at the anode, methanol is oxidized into CO_2 while concurrently generating electrons and protons. On the cathode side of the fuel cell, reduction of oxidants occurs. Oxygen enters the chamber where it combines with protons and electrons in an oxygen reduction reaction (ORR). Conductive ions migrate within the electrolyte that separates the cathode from the anode. Among the five electrolyte technologies, the proton exchange membrane (PEM) and the anion exchange membrane (AEM) play a crucial role in PEMFC [144], DMFC [145], DEFC [146], MFC [147], AEMFC [148] and DBFC [149] applications. The simple and efficient PEM and the low-cost AEM demonstrate strong potential for commercialization.

Due to the significant advantages of TMDs, such as exceptional mechanical performance, thermal stability, and resistance to methanol, extensive research efforts have been devoted to exploring their application in typical cathodic and anodic reactions and electrolytes. This section will focus on the research progress of tailored nanostructures of TMDs in these modules.

4.1. Cathode catalysts for ORR

The cathodes of these energy devices all involve ORR. Pt/C is widely employed as the most prevalent ORR catalyst due to its

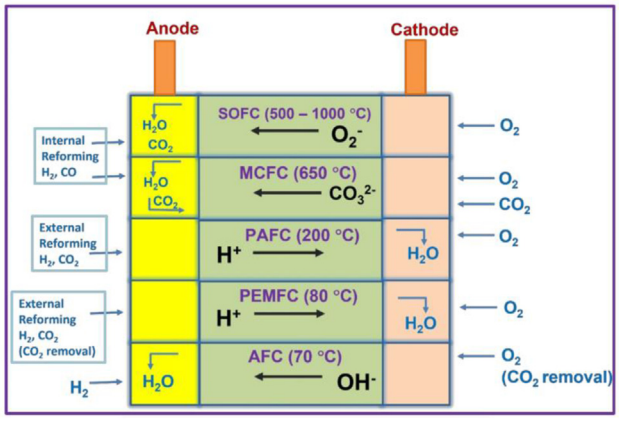

Fig. 7. Different kinds of fuel cells. Reproduced from the study by Vinodh et al. [150] with permission from MDPI.

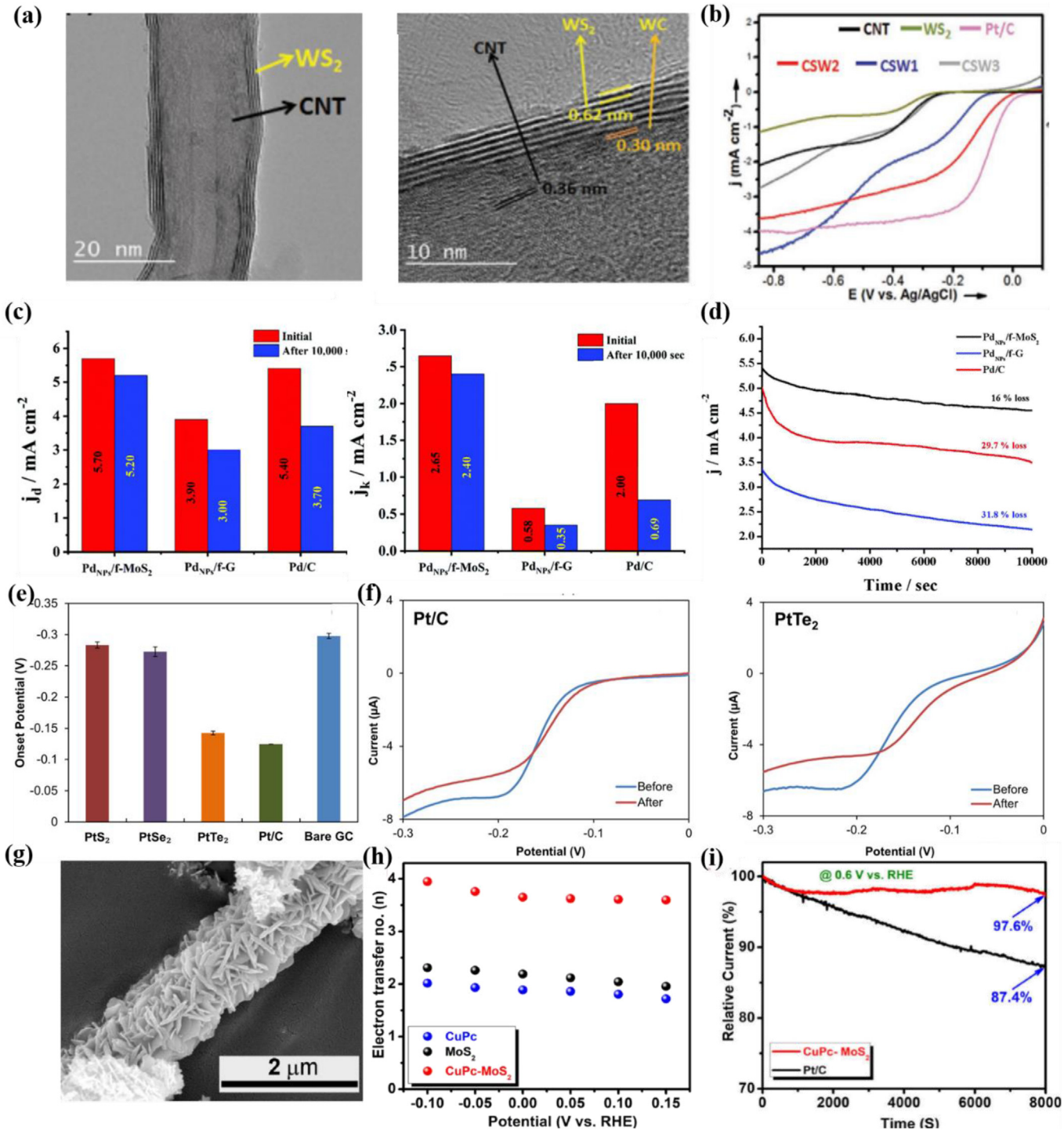

Fig. 8. Enhancement of ORR performance by multi-dimensional structures of TMDs. (**a**) HRTEM images of the WS_2-CNT hybrid NT and WC bond. (**b**) Linear sweep voltammetry of the different as synthesized samples. (a–b) Reproduced from the study by Tiwari et al. [153] with permission from the John Wiley and Sons. (**c**) Diffusion limited and kinetic current density values of Pd NPs/f-MoS_2 and Pd/C. (d) ORR chronoamperometric response for Pd NPs/f-MoS_2 and Pd/C at −0.45 V (vs. Hg/HgO) for 10 000 s. (c–d) Reproduced from the study by Perivoliotis et al. [159] with permission from the Royal Society of Chemistry. (**e**) Onset potentials for ORR on Pt dichalcogenides, Pt/C and bare GC using the potential at which 10% of the maximum current density is achieved. (**f**) The respective LSVs are recorded before and after performing 100 cycles of CV in a potential window of −50 to −250 mV. Potentials are with respect to the Ag/AgCl reference electrode. (e–f) Reproduced from the study by Rosli et al. [160] with permission from the American Chemical Society. (g) FESEM images of CuPc-MoS_2 hybrid. (**h**) Electron transfer no. at different potential. (i) Chronoamperometric stability of CuPc-MoS_2 and Pt/C. (g–i) Reproduced from the study by Samanta et al [161] with permission from Elsevier.

exceptional activity [151]. But the cathode often operates under high potential and in a strong acid/alkali environment, leading to severe electrochemical corrosion of the carbon black carrier. This corrosion results in dissolution or agglomeration of surface Pt particles, thereby diminishing both the activity and stability of the catalyst [152]. Consequently, researchers expected to find a highly active and corrosion-resistant ORR catalyst to prolong the life of energy devices. Among diverse materials, TMD materials offer new

opportunities for ORR catalyst due to their high surface area, high charge transfer, and stability in polar solvents.

1D structures like NTs and NSs, characterized by anisotropy, unique curling structure, and internal voids, show excellent catalytic activity that can rival noble metals Pt and Pt-based materials [23]. Anand P. Tiwari et al. [153] synthesized a WS_2-CNT hybrid nanotube structure bonded by tungsten carbide (WC) (Fig. 8a). This hybrid hierarchy was synthesized step by step through the growth of WS_2 nanosheets on CNTs using WC crystal structure. The limitation of non-close interaction between TMD and carbon materials is thus overcome. The hybrid samples containing 4–5 layers of WS_2 exhibited an initial potential of −11 mV (Fig. 8b) and an electron transfer number of 3.86 for the electrodes, close to commercially available Pt/C electrodes. Chemical bonding between W and C was key in providing an effective electron transfer pathway via spin polarization. It is worth noting that after 15 h of catalytic activity, the structural characterization of hybrid NTs through XRD, TEM, and SEM reveals that the WS_2-CNT hybrid structure remains unchanged, which fully indicates the long-term stability. Synthesis approaches for such hybrid NTs typically rely on 1D building blocks [154]. However, Chenyang Zhao et al. [155] synthesized MoS_2/nitrogen-doped carbon hybrid NTs (MoS_2/C HNT) using a one-pot method where the oxygen-containing MoS_2 monolayer was embedded in highly conductive nitrogen-dope CNTs. The hybrid NTs possess high ionic and electronic conductivity due to the large surface area and synergistic effect between doped N and MoS_2. The linear sweep voltammetry (LSV) polarization curve showed that the initial potential of the catalyst was 0.91 V and the half-wave potential was 0.82 V, which was close to Pt/C (0.97 and 0.84 V). The relative current density remains above 80% even after a chronoamperometric test lasting for 36 000 s, surpassing that of Pt/C. These findings suggest that MoS_2/C HNT holds great promise as a precious metal-free ORR catalyst. Although research on the NSs of TMDs has been extensively reported, it has mainly focused on photoelectric devices [156], with limited studies on catalytic applications for fuel cells.

2D materials with sheet-like structures are ideal supports for metal catalysts in ORR, owing to their larger surface area, uniform exposed lattice planes, and tunable electronic states [157]. Graphene nanosheets serve as a typical representative with excellent electrical conductivity up to 10^6 S/cm [158], but TMD materials represent higher stability than graphene and have emerged as promising alternatives. Dimitrios K. Perivoliotis et al. [159] used covalently functionalized MoS_2 nanosheets with 1,2-dithiolane derivatives (f-MoS_2) as substrates for immobilizing Pd NPs. The resulting hybrid material (Pd NPs/f-MoS_2) showed significantly enhanced electrocatalytic activity for ORR under alkaline conditions. The Pd NPs/f-MoS_2 exhibited a diffuse-limited current density of 5.70 mA/cm^2 and a kinetic current density of 2.65 mA/cm^2 at −60 mV (vs. Hg/HgO), which was better than the reference Pd/C (Fig. 8c). Durability experiments consistently demonstrated that after 10 000 s chronoamperometric test, the Pd NPs/f-MoS_2 retained 84% of its initial current response, while Pd/C experienced activity losses of 29.7% (Fig. 8d). The high concentration of d electrons on the MoS_2 surface supplies an effective synergistic interaction for the stabilization of the NPs, bringing about the noteworthy durability of the Pd NPs/MoS_2 catalyst. Apart from traditional TMDs, Nur Farhanah Rosli et al. [160] also discovered that $PtTe_2$ had an initial potential close to that of Pt/C with a minimal potential difference of only 0.018 V (Fig. 8e). This high ORR performance can be attributed to its metallic properties. Interestingly, after subjecting both $PtTe_2$ and Pt/C to 100 cyclic voltammograms in the negative window potential range of −50 to −250 mV, it was observed that the starting potential of $PtTe_2$ decreased by 34 mV while the starting potential of Pt/C decreased by 28 mV (Fig. 8f), indicating comparable ORR stability between these two materials.

The advantage offered by 3D nanoscale architectures lies in their ability to create richer interfaces for combining component strengths and shortening ion diffusion paths. Most commonly used structures involve constructing nanoscale 2D TMD nanosheets on conductive substrates or carbonaceous materials. Madhupriya Samanta et al. [161] employed a two-step simple hydrothermal method for growing uniform and dense high-crystallinity MoS_2 nanosheet arrays on copper phthalocyanine microrods (CuPc-MoS_2) (Fig. 8g). It was found that CuPc-MoS_2 efficiently reduced O_2 through the 4-electron pathway (Fig. 8h) and showed a mere 2.4% current attenuation after 8 000s of chronoamperometry response testing whereas 12.6% was observed for Pt/C with respect to initial current (Fig. 8i). The vertically distributed nanosheets in CuPc-MoS_2 provide fully exposed active sites for efficient ORR and facilitate mass/electron transfer. Similarly, researchers have also vertically grown high-density 2D MoS_2 nanosheets on carbon nanospheres [162], graphene nanosheets [163], Co@Co_9S_8 core-shell structures [164], and micro TiO_2 hollow spheres [165]. These

Table 2
Comparison of the catalytic performances involving MoS_2-based materials employed for ORR.

Dimension	Catalysts	Morphology	Onset potential (mV vs. RHE)	No. of electron transfer	Cycling stability	Electrolyte	Ref.
1D	MoS_2/C HNT	Nanohybrid	910	4.07	36 000 s	0.1 M KOH	[155]
	WS_2/CNT	Nanohybrid	−11 (vs. Hg/HgO)	3.86	60 000 s	0.1 M KOH	[153]
2D	MoS_2	Nanosheets	780	2.71	/	0.1 M KOH	[166]
	MoS_2	Nanosheets	100 (vs. SCE)	3.96	/	0.1 M H_2SO_4	[167]
	P-doped MoS_2	Nanosheets	960	3.60	10 000 s	0.1 M KOH	[168]
	O-doped MoS_2	Nanosheets	940	3.49	10 000 s	0.1 M KOH	[169]
	Ag–MoS_2	Nanohybrid	900	3.98	2000 cycles	0.1 M KOH	[166]
	MoS_2/rGO	Nanohybrid	800	3.00–3.32	/	0.1 M KOH	[170]
	Ni_3S_2/MoS_2	Nanosheets	950	3.99	6000 cycles	0.1 M KOH	[171]
	hBN/MoS_2	Heterostructure	800	4.00	2000 cycles	0.1 M KOH	[172]
	MoS_2/N-graphene	Nanohybrid	−1200 (vs. SCE)	3.75–3.90	/	0.1 M KOH	[173]
	Pt/MoS_2-rGO	Nanohybrid	900	/	10 000 cycles	0.1 M $HClO_4$	[174]
	Pd NPs/f-MoS_2	Nanohybrid	−66 (vs. Hg/HgO)	3.60–4.00	10 000 s	0.1 M KOH	[159]
	$PdSe_2$	Nanosheets	/	3.67	28 800 s	0.1 M KOH	[175]
	$PtTe_2$	Nanosheets	−18 (vs. Ag/AgCl)	/	2000 cycles	0.1 M KOH	[160]
3D	MoS_2	Nanoflowers	−140 (vs. Ag/AgCl)	/	2000 cycles	0.1 M KOH	[176]
	MoS_2/CNT	Nanohybrid	650	3.80–3.95	50 400 s	0.1 M KOH	[177]
	CuPc/MoS_2	Heterostructure	750	3.90	8000 s	0.1 M KOH	[161]
	MoS_2/graphene	Nanoflowers	840	3.60	5000 cycles	0.1 M KOH	[163]
	Co,Nb–MoS_2/TiO_2 HSs	Hollow spherical structure	810	3.96	60 000 s	0.1 M KOH	[165]
	Co_9S_8/Co_9S_8/MoS_2	Core-shell structure	/	~4.00	43 200 s	0.1 M KOH	[164]

Table 3
Comparison of the catalytic performances involving MoS_2-based materials employed for MOR.

Dimension	Catalysts	Morphology	Specific/mass activity/current density	Cycle stability	Electrolyte	Ref.
1D	Pt−CdS/MoS_2	Nanocomposite	1.13 mA/cm^2	79% after 400 cycles	1.0 M KOH +1.0 M CH_3OH	[180]
	Co−$PtTe_2$	Nanorods	8.3 mA/cm^2	74.8% after 500 cycles	0.1 M $HClO_4$ + 0.5 M CH_3OH	[178]
2D	Ni−MoS_2/MXene	Nanohybrid	7.7 mA/cm^2	78.4% after 500 cycles	0.1 M KOH + 1.0 M CH_3OH	[181]
	Pd−MoS_2	Nanosheets	433.5 mA/mg_{Pt}	/	0.5 M KOH + 1.0 M CH_3OH	[182]
	ReS_2/rGO	Nanocomposite	198 μA/cm^2 vs. Ag/AgCl	64% after 2500 s	0.1 M NaOH +0.5 M CH_3OH	[183]
	Au@Pt/MoS_2	Nanohybrid	6.24 A/mg_{Pt}	/	0.5 M NaOH + 1.0 M CH_3OH	[184]
3D	MoS_2/NiSi@SOD	Nanocomposite	46.9 mA/cm^2	/	1.0 M NaOH + 10.0 M CH_3OH	[185]
	MoS_2/Ni foam	Nanohybrid	73 vs Ag/AgCl	80% after 5000 s	0.1 M NaOH + 0.5 M CH_3OH	[179]
	Co_9S_8@MoS_2	Nanohybrid	121.4 mA/cm^2 vs Ag/AgCl	93.6% after 3000 s	1.0 M NaOH + 0.5 M CH_3OH	[186]
	MoS_2/Ni_3S_2/Ni foam	Nanohybrid	805.4 mA/mg_{Pt}	95.4% after 1000 cycles	1.0 M KOH + 1.0 M CH_3OH	[187]
	Pt/MoS_2/CNX	Nanocomposite	1030.2 mA/mg_{Pt}	/	0.5 M H_2SO_4 + 0.5 M CH_3OH	[188]
	Rh/MoS_2-RGO	Nanohybrid	1.57 mA/cm^2	/	1 M H_2SO_4 + 2 M CH_3OH	[189]
	MoS_2@CoNi-ZIF	Nanocomposite	229.32 mA/g	/	1.0 M KOH + 0.5 M CH_3OH	[190]

3D structures have demonstrated excellent electrocatalytic performance and high stability in electrochemical reactions.

Table 2 lists the TMD-based ORR catalysts with different dimensions. Overall, the improved ORR activity and stability observed in the catalytic layer relies on the chemical stability of TMDs, the active sites provided by TMDs and the possible synergistic interaction between TMDs and the substrate.

4.2. Anode catalysts for MOR

The fuel oxidation takes place at the anode of the fuel cell. In this section, by taking a typical methanol fuel as an example, the application of TMD materials in methanol electro oxidation (MOR) was introduced. The commonly employed MOR catalyst is noble metal-based material, which has low electrocatalytic activity towards the oxidation of small organic molecules such as alcohols, and is easily poisoned by oxidized intermediate species such as CO [143]. Therefore, it is important to study the anodic catalysts with high electrocatalytic activity for the oxidation of small organic molecules of alcohols and the anti-toxicity of oxidation intermediates. Among diverse types of materials, TMDs are favored due to properties such as tolerance to CO poisoning, high surface area, and high stability. Table 3 lists the TMD-based MOR catalysts with different dimensions. TMDs, represented by MoS_2, are used to load and disperse metal catalysts. In these research works, the electronic interaction between metal NPs and MoS_2 nanosheets adjust the surface electronic structure, thus improving the uniformity of metal NPs dispersed on the carrier surface. This structure effectively alleviates the issues of nanoparticle shedding and agglomeration.

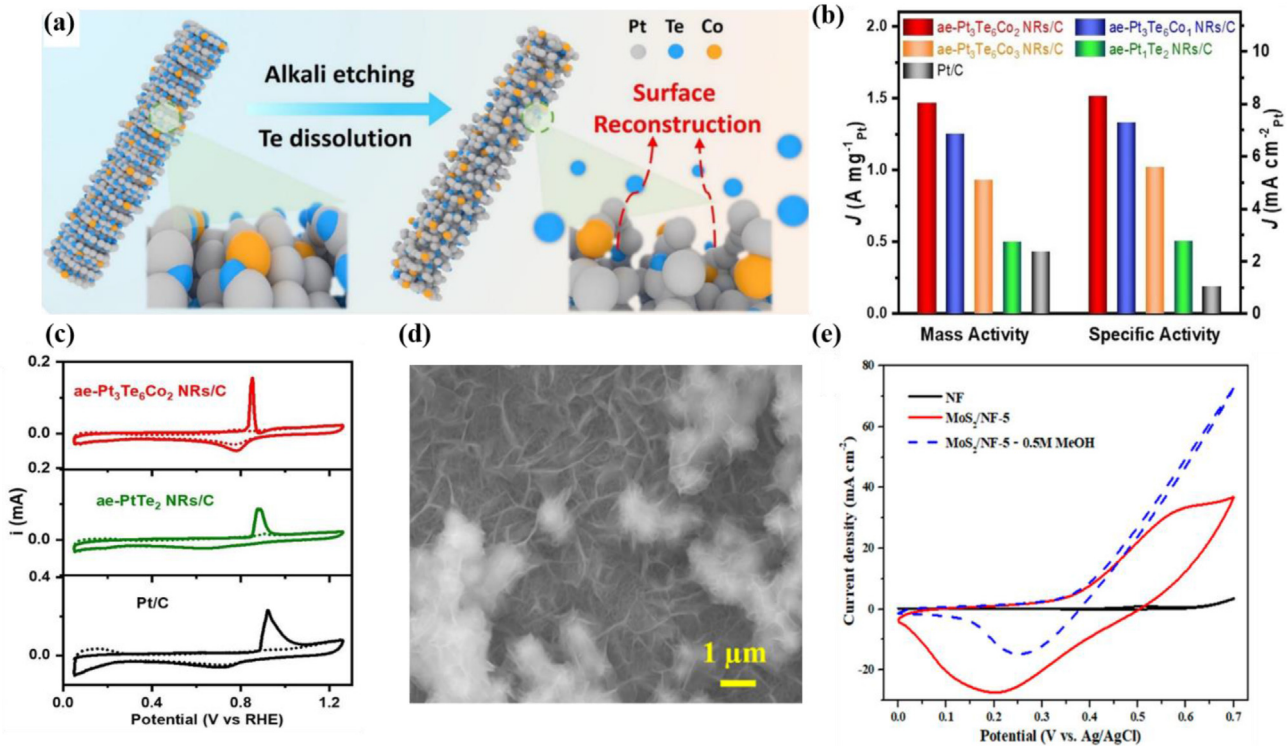

Fig. 9. Enhancement of MOR performance by multi-dimensional structures of TMDs. (**a**) Schematic illustrating the surface reconstruction of PtTeCo nanorods by alkali etching. (**b**) Mass activities and specific activities of ae-PtTeCo NRs/C with various atomic ratio, ae-$PtTe_2$ NRs/C, and commercial Pt/C in 0.1M $HClO_4$ and 0.5 M CH_3OH solution. (**c**) CO stripping experiments of different catalysts. (a−c) Reproduced from the study by Li et al. [178] with permission from Elsevier. (**d**) High-magnification images of MoS_2/NF-5. (**e**) CV plots of MoS_2/NF-5 electrodes in 0.1 M NaOH with and without 0.5M MeOH at 30 mV/s. (d−e) Reproduced from the study by Gopalakrishnan et al. [179] with permission from the American Chemical Society.

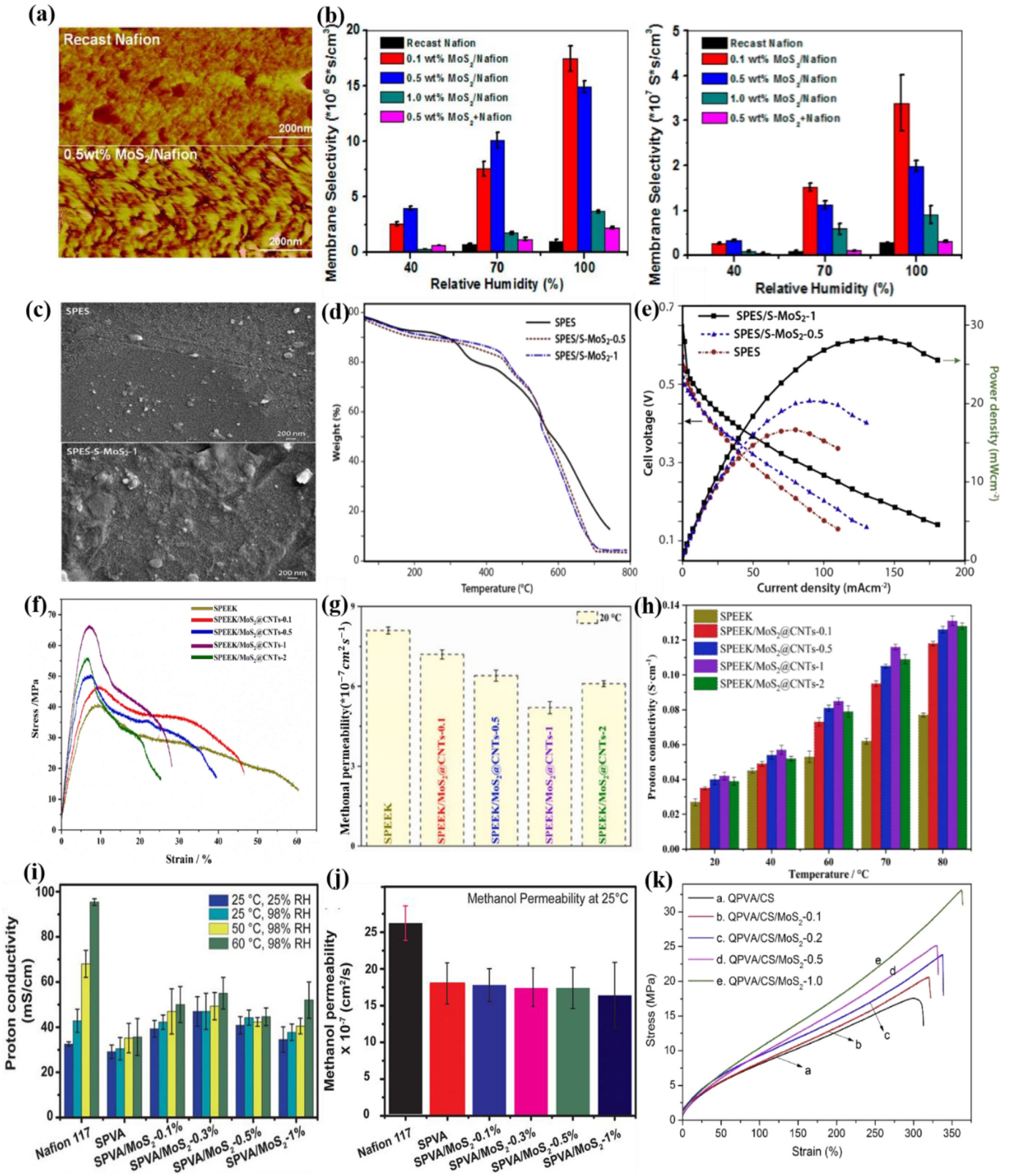

Fig. 10. The addition of TMD can enhance the performance of PEM and AEM. (**a**) AFM images of the recast nafion membrane and the 0.5 wt% MoS_2/nafion composite membrane. (**b**) Membrane selectivity of the recast nafion and MoS_2/nafion composite membranes under 25 °C and 50 °C. (a–b) Reproduced from the study by Feng et al. [191] with permission from the American Chemical Society. (**c**) FESEM images of pure SPES and SPES/S–MoS_2-1 nanocomposite membrane. The membranes were named as SPES/S–MoS_2-x, in which x (x = 0.5, 1) denotes different percentages of S–MoS_2 weight in the whole membrane. (d) TGA graph of SPES/S–MoS_2 nanocomposite membranes. (**e**) Single cell performance of SPES and SPES/S–MoS_2 nanocomposite membranes in DMFC. (c–e) Reproduced from the study by Divya et al. [192] with permission from Elsevier. (**f**) Tensile stress-strain curves of the membranes. The membranes were named as SPEEK/MoS_2@CNTs-x, in which x (x = 0.1, 0.5, 1 and 2) denotes different percentages of MoS_2@CNTs weight in the whole membrane. (**g**) Methanol permeability of pristine SPEEK and composite membranes. (h) Proton conductivity of membranes at different temperature. (f–h) Reproduced from the study by Zhong et al. [193] with permission from Elsevier. (**i**) Proton conductivity of the membranes. (**j**) Methanol permeability of the membranes at 25 °C. (i–j) Reproduced from the study by

In addition to being used as a carrier in the catalytic reaction, TMDs themselves can also be used as catalysts. Jie Li et al. [178] designed a metal-modified and defect-rich $PtTe_2$ nanorod (ae-$Pt_3Te_6Co_2$ NRs/C) (Fig. 9a) to overcome the CO poisoning problem. The ae-$Pt_3Te_6Co_2$ NRs/C achieved the highest mass activity of 1.47 A/mg_{Pt} and specific activity of 8.3 mA/cm^2 at 1.0 V vs RHE, which were 3.4 and 8.1 times higher than commercial Pt/C catalysts, respectively (Fig. 9b). More importantly, ae-$Pt_3Te_6Co_2$ NRs/C exhibited an initial CO oxidation potential of 889 mV, lower than that of Pt/C at 922 mV (Fig. 9c). The results show that modified Co and defective Pt sites are beneficial to CO oxidation and reduce catalyst poisoning. This overall enhancement in catalytic performance is inextricably linked to its 1D structure with abundant surface defects. The construction of 3D customized TMD nanostructures on the surface of metal catalysts shows more stacking ways of TMD materials for various electrochemical applications. Arthi Gopalakrishnan et al. [179] grew vertically aligned and folded molybdenum sulfide nanosheets on porous nickel foam (MoS_2/NF) (Fig. 9d), exhibiting a high current density of 73 mA/cm^2 at 0.7 V (Fig. 9e). At the same time, the I_f/I_b value of MoS_2/NF electrocatalyst was 5.1, indicating that the catalyst has a high tolerance to CO. This is closely related to the high electrocatalytic activity, the strong ability to resist CO poisoning, and the larger surface area of 3D TMD nanostructures.

In short, the customized TMDs with different dimensions provide MOR with fast charge transfer, a certain degree of resistance to CO poisoning and enhanced interaction with carbon support, which helps to prevent catalyst agglomeration and shedding problems during electrocatalysis process.

4.3. PEM and AEM electrolyte

PEM and AEM play a vital role in transferring ions and separating gas. At present, PEM mainly uses nafion membrane. Nafion membrane suffers reduced proton conductivity at a higher temperature, requiring noble metal catalyst, and catalyst poisoning by CO. Non-fluorinated polymers are a promising substitute [150]. AEM is mainly composed of anionic conductive groups and a specific polymer skeleton. A variety of polymer materials including polyether sulfone (PES), polyether ether ketone (PEEK) and polyvinyl alcohol (PVA) can be used as the main chain of PEM and AEM.

TMD is expected to improve the performance of PEM and AEM due to its excellent proton conductivity and high temperature stability. The most essential transport characteristics of PEM are proton conductivity and methanol permeability. The ratio of them is called selectivity. Ideally, PEM should only allow the transfer of protons from the anode to the cathode but not allow fuel to cross. Although nafion-based PEMs have excellent proton conductivity, they also have severe fuel crossover because they are transported through almost the same path within the nafion matrix. Kai Feng et al. [191] fabricated MoS_2/nafion composite films with two orders of magnitude higher selectivity than pure nafion films. MoS_2 nanosheets selectively grew around the MoS_2/nafion composite membrane ion clusters, which promoted aggregation, resulting in better connectivity of these ion clusters. AFM images showed that the 0.5 wt% MoS_2/Nafion composite membrane had larger ion clusters and better connectivity, which greatly improved PEM proton conductivity (Fig. 10a). At the same time, the presence of MoS_2 in the ion channel increased the curvature of the membrane, which effectively prevented the fuel migration through the PEM (Fig. 10b).

PEM and AEM based on PEEK, PES, PVA and other basic polymers have excellent chemical, mechanical and thermal stability, and shows great proton and ion conductivity and selectivity. Many kinds of new PEM have been developed by embedding TMD into the substrate. Sulfonate PES (SPES) has a very high dipole moment, which is conducive to proton conduction. Kumar Divya et al. [192] successfully prepared SPES/S−MoS_2 nanocomposite PEM as an alternative to commercially available nafion with high cost. S−MoS_2 nano-filler had excellent dispersion ability in SPES matrix, as shown in Fig. 10c, the dark area represented the polymer and the white area represented the S−MoS_2 nanofiller. Compared with SPES films, the thermal stability, tensile strength, hydrophilicity, proton conductivity and selectivity of SPES/S−MoS_2 composite films were significantly improved. The fuel concentration on the water side was measured every 6 h. SPES/S−MoS_2-1 showed a fuel oxidation current of 0.007 mA that was much lower than the 0.018 mA of the SPES film. It showed that the addition of S−MoS_2 nano-filler increased the tortuosity of the film and effectively block the fuel flow. As shown in Fig. 10d, the addition of S−MoS_2 nanofillers enhanced the thermal stability of SPES films. This may be due to the strong electrostatic attraction between SPES and S−MoS_2 and the high thermal stability of MoS_2. The pure SPES film showed lower DMFC performance with a peak power density of 16.72 mW/cm^2, while the SPES/S−MoS_2-1 composite film showed the highest DMFC performance with a peak power density of 28.28 mW/cm^2 (Fig. 10e). By incorporating 1D CNTs and 2D MoS_2 nanosheets into the sulfonated PEEK (SPEEK), Fei Zhong et al. [193] prepared the SPEEK/MoS_2@CNTs composite film. It showed an improvement in mechanical properties (Fig. 10f) and a significant reduction in fuel permeability (Fig. 10g). At 80 °C, the SPEEK/MoS_2@CNTs-1 composite membrane had the maximum proton conductivity of 0.131 S/cm, which was 1.7 times of the original SPEEK membrane (Fig. 10h). The addition of 1D CNT made ion clusters construct a proton transfer pathway along the nanotube interconnection, thus improving the overall proton transport performance. SPEEK/MoS_2@CNTs-1 composite membrane showed excellent fuel cell performance, with a peak power density of 98.5 mW/cm^2 at 70 °C. The presence of MoS_2 nanosheets broke the strong vdW interaction between CNTs and avoided the aggregation of CNTs in the SPEEK matrix. Recently, by solution-casting the exfoliated MoS_2 nanosheets into a sulfonated PVA (SPVA) matrix, Pankaj Kumar et al. [194] prepared SPVA/MoS_2 composite films. It displayed a reduction in fuel crossover and an improvement in proton conductivity. SPVA/MoS_2 films with 0.3 wt% MoS_2 had the highest proton conductivity of 48 ± 7 mS/cm, which was 1.8 times of pure SPVA (Fig. 10i). Compared with the original SPVA membrane, the composite membrane had better resistance to fuel cross (Fig. 10j). For AEM, the addition of TMD as inorganic filler is also an effective method to improve the ion conductivity, thermal stability and fuel barrier properties of polymer films. Xiancai Jiang et al. [195] prepared QPVA/CS/MoS_2 AEM. The addition of MoS_2 improved the thermal stability, mechanical strength and swelling rate of the composite film, and with the increase of MoS_2 content, the fuel permeability of the composite film gradually decreased, but the ion conductivity gradually increased. Compared with 17.6 MPa of pure QPVA/CS film, the tensile strength of QPVA/CS/MoS_2 film was significantly increased, and the tensile strength of QPVA/CS/MoS_2-1 film was increased to 33.1 MPa (Fig. 10k). QPVA/

Kumar et al. [194] with permission from the American Chemical Society. (**k**) Tensile stress-strain curves of the membranes. The membranes were named as QPVA/CS/MoS_2-x, in which x (x = 0.1, 0.2, 0.5 and 1) denotes different percentages of MoS_2 nanosheets weight in the whole membrane. Reproduced from the study by Jiang et al. [195] with permission from Elsevier.

CS/MoS_2-0.2 films had the highest ionic conductivity of 3.153×10^{-2} S/cm. The fuel permeability of the QPVA/CS/MoS_2-1 composite membrane was the lowest, which was 0.210×10^{-7} cm^2/s.

The composite membrane prepared with TMDs as inorganic filler has excellent properties. At the same time, TMDs nanosheets can form a good dispersion in water and other solvents. Therefore, it can be prepared into a film by simple chemical procedures such as rotation and impregnation, which reduces the preparation cost. TMDs can enhance the ion transport performance of the composite membrane, thereby enhancing the cell efficiency and shortening the response time. TMDs can enhance the mechanical strength and thermal stability of the composite film so that it is not easy to deform or degrade, thus extending the service life of the battery. TMDs can enhance the selectivity of the composite film and improve the energy conversion efficiency of the battery. In short, the application of TMD to fuel cells can improve its efficiency, performance and reliability, reduce costs and maintenance requirements, and promote its wide application in various application fields.

5. Conclusions and outlook

To sum up, recent advances in TMD materials from monomer synthesis to assembly into tailored nanostructures of different dimensions are summarized. Typical structures contain 1D NTs or NSs formed from folded or rolled TMD sheets, large 2D films grown directly or assembled after monomer synthesis and 3D nanostereostructure synthesized by hydrothermal synthesis. As a result, bright spots with controllable size, surface and morphology allow TMDs to suit the material requirements of different components in fuel cells. As catalyst carriers, it achieves efficient electron transport, superior stability and fine mass transfer effect. Embedding TMDs as inorganic filler, the PEM matrix reduces fuel crossing and improves membrane selectivity by increasing curvature. Multidimensional nanostructures of TMDs provide an unprecedented material platform for the energy sector. However, the controllability of monomer preparation and the complexity of actual conditions have frustrated the application of TMDs materials. In order to overcome the disconnection between material scale and application scale, we propose the following perspectives:

(1) It is still difficult to control the synthesis of monomers precisely. Diverse NTs differ in species, number of tube walls, diameter and chiral structure. In this regard, fine structure control such as chiral control is a promising direction. In the future, more in-depth mechanistic studies on the growth process of NTs based on solid catalysts are needed to put forward more reasonable theories to explain and predict their growth behavior.
(2) The ideal preparation combines precise structural control with batch production. In addition to controlling the microstructure, it is equally important to construct macroscopic structural aggregation, such as horizontal arrays, vertical arrays, films, and gels. Fluidized bed reactors have been widely used for the large-scale production of WS_2 NTs, but research on other TMD materials using this method is still limited. Furthermore, researchers need to pay more attention to issues such as wall number control, spinnability, and array density, which play a dominant role in industrial applications. Comprehensive solutions to these problems will promote the practical application of the nanotube family.
(3) The 3D architecture of TMDs needs to be fully explored. In 3D TMD architectures, the restacking of the TMD nanosheets is effectively suppressed and more active sites are exposed to electrochemical reactions. However, most 3D TMD structures are built from semiconductor TMDs such as MoS_2. Structures based on metallic TMDs are rare. It has been shown that metallic TMDs have abundant base surface, more active edge sites and better electron transport. The exploration of 3D architecture may lead to breakthroughs in electrochemical properties.
(4) In the application of fuel cells, the effect of the complex solution environment on the material should be considered. Metal catalysts of different dimensions are loaded on TMDs to construct composite catalysts with small structures and large interfaces. Extensive work has shown that TMDs as supports improve catalytic performance and effectively enhance the durability of metal catalysts. However, in real electrocatalytic reaction processes, doping and composites affect the surface properties of TMDs, strong acid or alkali solutions and external electric fields can also change the friction and adhesion properties of materials. Therefore, further research on the complex interfacial chemistry of electrochemical reaction processes will benefit the study of this catalytic layer.

Overall, the complex and changeable nanostructures assembled by the TMD family have a wide range of application prospects in fuel cells. Although challenges such as high-purity batch production, complex interfacial chemistry, and lower cost remain, TMDs are hopeful to truly meet people's expectations in sustainable energy conversion and become the next generation of key materials with the gradual deepening of research.

CRediT authorship contribution statement

Yani Dong: Writing – original draft. **Zongying Ma:** Writing – original draft. **Isabel Lopez:** Writing – review & editing. **Travis Shihao Hu:** Writing – review & editing. **Qizhi Dong:** Supervision. **Song Liu:** Supervision.

Declaration of competing interest

The authors declare that they have no known competing financial interests or personal relationships that could have appeared to influence the work reported in this article.

Data availability

The authors do not have permission to share data.

Acknowledgments

The work gratefully acknowledges financial support from the National Natural Science Foundation of China (No. 22175060, 21975067), Natural Science Foundation of Hunan Province of China (2021JJ10014, 2021JJ30092) and U.S. National Science Foundation (NSF Award No. 2004251).

References

[1] N.D. Popovich, D. Rajagopal, E. Tasar, A. Phadke, Economic, environmental and grid-resilience benefits of converting diesel trains to battery-electric, Nat. Energy 6 (2021) 1017–1025, https://doi.org/10.1038/s41560-021-00915-5.
[2] I. Staffell, D. Scamman, A. Velazquez Abad, P. Balcombe, P.E. Dodds, P. Ekins, N. Shah, K.R. Ward, The role of hydrogen and fuel cells in the global energy system, Energy Environ. Sci. 12 (2019) 463–491, https://doi.org/10.1039/c8ee01157e.
[3] S. Fukuzumi, Production of liquid solar fuels and their use in fuel cells, Joule 1 (2017) 689–738, https://doi.org/10.1016/j.joule.2017.07.007.

[4] Z.P. Cano, D. Banham, S. Ye, A. Hintennach, J. Lu, M. Fowler, Z. Chen, Batteries and fuel cells for emerging electric vehicle markets, Nat. Energy 3 (2018) 279–289, https://doi.org/10.1038/s41560-018-0108-1.
[5] N. Guerrero Moreno, M. Cisneros Molina, D. Gervasio, J.F. Pérez Robles, Approaches to polymer electrolyte membrane fuel cells (PEMFCs) and their cost, Renew. Sustain. Energy Rev. 52 (2015) 897–906, https://doi.org/10.1016/j.rser.2015.07.157.
[6] Y. Gu, Y. Liu, X. Cao, Evolving strategies for tumor immunotherapy: enhancing the enhancer and suppressing the suppressor, Natl. Sci. Rev. 4 (2017) 161–163, https://doi.org/10.1093/nsr/nwx032.
[7] Q. Meyer, Y. Zeng, C. Zhao, In situ and operando characterization of proton exchange membrane fuel cells, Adv. Mater. 31 (2019) 1901900, https://doi.org/10.1002/adma.201901900.
[8] J.-S. Lai, M.W. Ellis, Fuel cell power systems and applications, Proc. IEEE 105 (2017) 2166–2190, https://doi.org/10.1109/jproc.2017.2723561.
[9] S.M. Ng, H. Wang, Y. Liu, H.F. Wong, H.M. Yau, C.H. Suen, Z.H. Wu, C.W. Leung, J.-Y. Dai, High-temperature anomalous Hall effect in a transition metal dichalcogenide ferromagnetic insulator heterostructure, ACS. Nano. 14 (2020) 7077–7084, https://doi.org/10.1021/acsnano.0c01815.
[10] Y. Xiong, H. Chen, D.W. Zhang, P. Zhou, Electronic and optoelectronic applications based on ReS_2, Phys. Status Solidi Rapid Res. Lett. 13 (2019) 1800658, https://doi.org/10.1002/pssr.201800658.
[11] H. Xu, H. Zhang, Y. Liu, S. Zhang, Y. Sun, Z. Guo, Y. Sheng, X. Wang, C. Luo, X. Wu, J. Wang, W. Hu, Z. Xu, Q. Sun, P. Zhou, J. Shi, Z. Sun, D.W. Zhang, W. Bao, Controlled doping of wafer-scale $PtSe_2$ films for device application, Adv. Funct. Mater. 29 (2018) 1805614, https://doi.org/10.1002/adfm.201805614.
[12] M. Wenda, D. Yan, L. Jihong, W. Yang, W. Tongzhou, Z. Xuerong, D. Yida, Recent strategies for improving the catalytic activity of ultrathin transition metal sulfide nanosheets toward the oxygen evolution reaction, Mater. Today Energy 40 (2024) 101492, https://doi.org/10.1016/j.mtener.2024.101492.
[13] L. Peng, Z. Fang, Y. Zhu, C. Yan, G. Yu, Holey 2D nanomaterials for electrochemical energy storage, Adv. Energy Mater. 8 (2017) 1702179, https://doi.org/10.1002/aenm.201702179.
[14] M. Zeng, Y. Xiao, J. Liu, K. Yang, L. Fu, Exploring two-dimensional materials toward the next-generation circuits: from monomer design to assembly control, Chem. Rev. 118 (2018) 6236–6296, https://doi.org/10.1021/acs.chemrev.7b00633.
[15] J. Khan, R.T.M. Ahmad, J. Tan, R. Zhang, U. Khan, B. Liu, Recent advances in 2D organic-inorganic heterostructures for electronics and optoelectronics, SmartMat 4 (2022) e1156, https://doi.org/10.1002/smm2.1156.
[16] W. Wang, F. Xiong, S. Zhu, J. Chen, J. Xie, Q. An, Defect engineering in molybdenum-based electrode materials for energy storage, eScience 2 (2022) 278–294, https://doi.org/10.1016/j.esci.2022.04.005.
[17] G.H. Jeong, S.P. Sasikala, T. Yun, G.Y. Lee, W.J. Lee, S.O. Kim, Nanoscale assembly of 2D materials for energy and environmental applications, Adv. Mater. 32 (2020) 1907006, https://doi.org/10.1002/adma.201907006.
[18] Y. Xiao, C. Xiong, M.-M. Chen, S. Wang, L. Fu, X. Zhang, Structure modulation of two-dimensional transition metal chalcogenides: recent advances in methodology, mechanism and applications, Chem. Soc. Rev. 52 (2023) 1215–1272, https://doi.org/10.1039/d1cs01016f.
[19] Q. Yun, Q. Lu, X. Zhang, C. Tan, H. Zhang, Three-dimensional architectures constructed from transition-metal dichalcogenide nanomaterials for electrochemical energy storage and conversion, Angew. Chem. Int. Ed. 57 (2018) 626–646, https://doi.org/10.1002/anie.201706426.
[20] L. Zhang, H.B. Wu, Y. Yan, X. Wang, X.W. Lou, Hierarchical MoS_2 microboxes constructed by nanosheets with enhanced electrochemical properties for lithium storage and water splitting, Energy Environ. Sci. 7 (2014) 3302–3306, https://doi.org/10.1039/c4ee01932f.
[21] P.p. Wang, H. Sun, Y. Ji, W. Li, X. Wang, Three-dimensional assembly of single-layered MoS_2, Adv. Mater. 26 (2013) 964–969, https://doi.org/10.1002/adma.201304120.
[22] B. Guo, K. Yu, H. Song, H. Li, Y. Tan, H. Fu, C. Li, X. Lei, Z. Zhu, Preparation of hollow microsphere@onion-like solid nanosphere MoS_2 coated by a carbon shell as a stable anode for optimized lithium storage, Nanoscale 8 (2016) 420–430, https://doi.org/10.1039/c5nr05595d.
[23] S. Aftab, M.Z. Iqbal, Y.S. Rim, Recent advances in rolling 2D TMDs nanosheets into 1D TMDs nanotubes/nanoscrolls, Small 19 (2022) 2205418, https://doi.org/10.1002/smll.202205418.
[24] R. Ghosh, M. Singh, L.W. Chang, H.-I. Lin, Y.S. Chen, J. Muthu, B. Papnai, Y.S. Kang, Y.-M. Liao, K.P. Bera, G.-Y. Guo, Y.-P. Hsieh, M. Hofmann, Y.-F. Chen, Enhancing the photoelectrochemical hydrogen evolution reaction through nanoscrolling of two-dimensional material heterojunctions, ACS. Nano. 16 (2022) 5743–5751, https://doi.org/10.1021/acsnano.1c10772.
[25] J. Su, G.D. Li, X.H. Li, J.S. Chen, 2D/2D heterojunctions for catalysis, Adv. Sci. 6 (2019), https://doi.org/10.1002/advs.201801702.
[26] M. Seol, M.H. Lee, H. Kim, K.W. Shin, Y. Cho, I. Jeon, M. Jeong, H.I. Lee, J. Park, H.J. Shin, High-throughput growth of wafer-scale monolayer transition metal dichalcogenide via vertical ostwald ripening, Adv. Mater. 32 (2020) 2003542, https://doi.org/10.1002/adma.202003542.
[27] Y. Zhang, L. Xu, W.R. Walker, C.M. Tittle, C.J. Backhouse, M.A. Pope, Langmuir films and uniform, large area, transparent coatings of chemically exfoliated MoS_2 single layers, J. Mater. Chem. C 5 (2017) 11275–11287, https://doi.org/10.1039/c7tc02637d.
[28] Z. Lai, Y. Chen, C. Tan, X. Zhang, H. Zhang, Self-assembly of two-dimensional nanosheets into one-dimensional nanostructures, Chem 1 (2016) 59–77, https://doi.org/10.1016/j.chempr.2016.06.011.
[29] M.K. Shahzad, F.H. Memon, F. Soomro, M. Iqbal, A. Ibrar, A.A. Memon, J.H. Lim, K.H. Choi, K.H. Thebo, MoS_2-based lamellar membranes for mass transport applications: challenges and opportunities, J. Environ. Chem. Eng. 11 (2023) 109329, https://doi.org/10.1016/j.jece.2023.109329.
[30] X. Hu, L. Yan, L. Ding, N. Zheng, D. Li, T. Ji, N. Chen, J. Hu, Structural regulation and application of transition metal dichalcogenide monolayers: progress and challenges, Coord. Chem. Rev. 499 (2024) 215504, https://doi.org/10.1016/j.ccr.2023.215504.
[31] X. Song, Z. Guo, Q. Zhang, P. Zhou, W. Bao, D.W. Zhang, Progress of large-scale synthesis and electronic device application of two-dimensional transition metal dichalcogenides, Small 13 (2017) 1700098, https://doi.org/10.1002/smll.201700098.
[32] W. Li, Y. Huang, Y. Liu, M.C. Tekell, D. Fan, Three dimensional nanosuperstructures made of two-dimensional materials by design: synthesis, properties, and applications, Nano. Today. 29 (2019) 100799, https://doi.org/10.1016/j.nantod.2019.100799.
[33] B.L. Li, J. Wang, H.L. Zou, S. Garaj, C.T. Lim, J. Xie, N.B. Li, D.T. Leong, Low-dimensional transition metal dichalcogenide nanostructures based sensors, Adv. Funct. Mater. 26 (2016) 7034–7056, https://doi.org/10.1002/adfm.201602136.
[34] N. Ullah, D. Guziejewski, A. Yuan, S.A. Shah, Recent advancement and structural engineering in transition metal dichalcogenides for alkali metal ions batteries, Materials 16 (2023) 2559, https://doi.org/10.3390/ma16072559.
[35] Y. Lv, P. Chen, J.J. Foo, J. Zhang, W. Qian, C. Chen, W.j. Ong, Dimensionality-dependent MoS_2 toward efficient photocatalytic hydrogen evolution: from synthesis to modifications in doping, surface and heterojunction engineering, Mater. Today. Nano. 18 (2022) 100191, https://doi.org/10.1016/j.mtnano.2022.100191.
[36] V. Yadav, S. Roy, P. Singh, Z. Khan, A. Jaiswal, 2D MoS_2-based nanomaterials for therapeutic, bioimaging, and biosensing applications, Small 15 (2019) 1803706, https://doi.org/10.1002/smll.201803706.
[37] X. Wu, H. Zhang, J. Zhang, X.W. Lou, Recent advances on transition metal dichalcogenides for electrochemical energy conversion, Adv. Mater. 33 (2021) 2008376, https://doi.org/10.1002/adma.202008376.
[38] Q. An, W. Xiong, F. Hu, Y. Yu, P. Lv, S. Hu, X. Gan, X. He, J. Zhao, S. Yuan, Direct growth of single-chiral-angle tungsten disulfide nanotubes using gold nanoparticle catalysts, Nat. Mater. (2023) 1–9, https://doi.org/10.1038/s41563-023-01590-5.
[39] S. Zhuo, Y. Xu, W. Zhao, J. Zhang, B. Zhang, Hierarchical nanosheet-based MoS_2 nanotubes fabricated by an anion-exchange reaction of MoO_3-amine hybrid nanowires, Angew. Chem. Int. Ed. 52 (2013) 8602–8606, https://doi.org/10.1002/anie.201303480.
[40] L. Zhang, Q. Hao, J. Liu, J. Zhou, W. Zhang, Y. Li, Rolling up of 2D nanosheets into 1D Nanoscrolls: visible-Light-Activated chemiresistors based on surface modified indium selenide with enhanced sensitivity and stability, Chem. Eng. J. 446 (2022) 136937, https://doi.org/10.1016/j.cej.2022.136937.
[41] Y. Zhao, H. You, X. Li, C. Pei, X. Huang, H. Li, Solvent-free preparation of closely packed MoS_2 nanoscrolls for improved photosensitivity, ACS Appl. Mater. Interfaces 14 (2022) 9515–9524, https://doi.org/10.1021/acsami.1c24291.
[42] J. Lee, J. Heo, H.Y. Lim, J. Seo, H. Park, Defect-induced in situ atomic doping in transition metal dichalcogenides via liquid-phase synthesis toward efficient electrochemical activity, ACS. Nano. 14 (2020) 17114–17124, https://doi.org/10.1021/acsnano.0c06783.
[43] X. Tong, Y. Zhao, Z. Zhuo, Z. Yang, S. Wang, Y. Liu, N. Lu, H. Li, T. Zhai, Dual-Regulation of defect sites and vertical conduction by spiral domain for electrocatalytic hydrogen evolution, Angew. Chem. Int. Ed. 61 (2021) e202112953, https://doi.org/10.1002/anie.202112953.
[44] S. Zhang, B.V.R. Chowdari, Z. Wen, J. Jin, J. Yang, Constructing highly oriented configuration by few-layer MoS_2: toward high-performance lithium-ion batteries and hydrogen evolution reactions, ACS. Nano. 9 (2015) 12464–12472, https://doi.org/10.1021/acsnano.5b05891.
[45] J. Peng, Z. Yu, J. Wu, Y. Zhou, Y. Guo, Z. Li, J. Zhao, C. Wu, Y.J.A.n. Xie, Disorder enhanced superconductivity toward TaS_2 monolayer, ACS. Nano. 12 (2018) 9461–9466, https://doi.org/10.1021/acsnano.8b04718.
[46] L. Zhang, G. Wang, Y. Zhang, Z. Cao, Y. Wang, T. Cao, C. Wang, B. Cheng, W. Zhang, X. Wan, Tuning electrical conductance in bilayer MoS_2 through defect-mediated interlayer chemical bonding, ACS. Nano. 14 (2020) 10265–10275, https://doi.org/10.1021/acsnano.0c03665.
[47] M. Kamitani, M.S. Bahramy, R. Arita, S. Seki, T. Arima, Y. Tokura, S. Ishiwata, Superconductivity in Cu_xIrTe_2 driven by interlayer hybridization, Phys. Rev. B 87 (2013) 180501, https://doi.org/10.1103/PhysRevB.87.180501.
[48] H. Kwon, K. Lee, J. Heo, Y. Oh, H. Lee, S. Appalakondaiah, W. Ko, H.W. Kim, J.W. Jung, H. Suh, Characterization of edge contact: atomically resolved semiconductor-metal lateral boundary in MoS_2, Adv. Mater. 29 (2017) 1702931, https://doi.org/10.1002/adma.201702931.
[49] J. Zhang, J. Wang, P. Chen, Y. Sun, S. Wu, Z. Jia, X. Lu, H. Yu, W. Chen, J. Zhu, Observation of strong interlayer coupling in MoS_2/WS_2 heterostructures, Adv. Mater. 28 (2016) 1950–1956, https://doi.org/10.1002/adma.201504631.
[50] S. Bertolazzi, J. Brivio, A. Kis, Stretching and breaking of ultrathin MoS_2, ACS. Nano. 5 (2011) 9703–9709, https://doi.org/10.1021/nn203879f.

[51] A. Castellanos-Gomez, M. Poot, G.A. Steele, H.S. Van Der Zant, N. Agraït, G. Rubio-Bollinger, Elastic properties of freely suspended MoS_2 nanosheets, Adv. Mater. 24 (2012) 772–775, https://doi.org/10.1002/adma.201103965.
[52] Y. Sun, J. Pan, Z. Zhang, K. Zhang, J. Liang, W. Wang, Z. Yuan, Y. Hao, B. Wang, J. Wang, Elastic properties and fracture behaviors of biaxially deformed, polymorphic $MoTe_2$, Nano Lett. 19 (2019) 761–769, https://doi.org/10.1021/acs.nanolett.8b03833.
[53] Y. Zhao, X. Luo, H. Li, J. Zhang, P.T. Araujo, C.K. Gan, J. Wu, H. Zhang, S.Y. Quek, M.S. Dresselhaus, Interlayer breathing and shear modes in few-trilayer MoS_2 and WSe_2, Nano Lett. 13 (2013) 1007–1015, https://doi.org/10.1021/nl304169w.
[54] Z. Zhang, Z. Tian, Y. Mei, Z. Di, Shaping and structuring 2D materials via kirigami and origami, Mater. Sci. Eng. R Rep. 145 (2021) 100621, https://doi.org/10.1016/j.mser.2021.100621.
[55] Z. Dai, N. Lu, K.M. Liechti, R. Huang, Mechanics at the interfaces of 2D materials: challenges and opportunities, Curr. Opin. Solid State Mater. Sci. 24 (2020) 100837, https://doi.org/10.1016/j.cossms.2020.100837.
[56] M.R. Vazirisereshk, K. Hasz, M.-Q. Zhao, A.C. Johnson, R.W. Carpick, A. Martini, Nanoscale friction behavior of transition-metal dichalcogenides: role of the chalcogenide, ACS. Nano. 14 (2020) 16013–16021, https://doi.org/10.1021/acsnano.0c07558.
[57] M. Rejhon, F. Lavini, A. Khosravi, M. Shestopalov, J. Kunc, E. Tosatti, E. Riedo, Relation between interfacial shear and friction force in 2D materials, Nat. Nanotechnol. 17 (2022) 1280–1287, https://doi.org/10.1038/s41565-022-01237-7.
[58] M. Liao, P. Nicolini, L. Du, J. Yuan, S. Wang, H. Yu, J. Tang, P. Cheng, K. Watanabe, T. Taniguchi, Ultra-low friction and edge-pinning effect in large-lattice-mismatch van der Waals heterostructures, Nat. Mater. 21 (2022) 47–53, https://doi.org/10.1038/s41563-021-01058-4.
[59] H. Du, Y. Kang, C. Xu, T. Xue, W. Qiu, H. Xie, Measurement and characterization of interfacial mechanical properties of graphene/MoS_2 heterostructure by Raman and photoluminescence (PL) spectroscopy, Opt Laser. Eng. 149 (2022) 106825, https://doi.org/10.1016/j.optlaseng.2021.106825.
[60] J. Yu, S. Kim, E. Ertekin, A.M. Van Der Zande, Material-dependent evolution of mechanical folding instabilities in two-dimensional atomic membranes, ACS Appl. Mater. Interfaces 12 (2020) 10801–10808, https://doi.org/10.1021/acsami.9b20909.
[61] D.A. Sanchez, Z. Dai, P. Wang, A. Cantu-Chavez, C.J. Brennan, R. Huang, N. Lu, Mechanics of spontaneously formed nanoblisters trapped by transferred 2D crystals, Proc. Natl. Acad. Sci. U.S.A. 115 (2018) 7884–7889, https://doi.org/10.1073/pnas.1801551115.
[62] H. Rokni, W. Lu, Direct measurements of interfacial adhesion in 2D materials and van der Waals heterostructures in ambient air, Nat. Commun. 11 (2020) 5607, https://doi.org/10.1038/s41467-020-19411-7.
[63] S.R. Na, Y. Kim, C. Lee, K.M. Liechti, J.W. Suk, Adhesion and self-healing between monolayer molybdenum disulfide and silicon oxide, Sci. Rep. 7 (2017) 14740, https://doi.org/10.1038/s41598-017-14921-9.
[64] J. Torres, Y. Zhu, P. Liu, S.C. Lim, M. Yun, Adhesion energies of 2D graphene and MoS_2 to silicon and metal substrates, Physica. Status. Solidi (A) - Applications. Materials. Science 215 (2018) 1700512, https://doi.org/10.1002/pssa.201700512.
[65] T. Arif, S. Yadav, G. Colas, C.V. Singh, T. Filleter, Understanding the independent and interdependent role of water and oxidation on the tribology of ultrathin molybdenum disulfide (MoS_2), Adv. Mater. Interfac. 6 (2019) 1901246, https://doi.org/10.1002/admi.201901246.
[66] T. Arif, G. Colas, T. Filleter, Effect of humidity and water intercalation on the tribological behavior of graphene and graphene oxide, ACS Appl. Mater. Interfaces 10 (2018) 22537–22544, https://doi.org/10.1021/acsami.8b03776.
[67] Y. Meng, J. Xu, Z. Jin, B. Prakash, Y. Hu, A review of recent advances in tribology, Friction 8 (2020) 221–300, https://doi.org/10.1007/s40544-020-0367-2.
[68] H. Lang, Y. Peng, G. Shao, K. Zou, G. Tao, Dual control of the nanofriction of graphene, J. Mater. Chem. C 7 (2019) 6041–6051, https://doi.org/10.1039/c9tc01148j.
[69] B. Shi, X. Gan, H. Lang, K. Zou, L. Wang, J. Sun, Y. Lu, Y. Peng, Ultra-low friction and patterning on atomically thin MoS_2 via electronic tight-binding, Nanoscale 13 (2021) 16860–16871, https://doi.org/10.1039/d1nr04252a.
[70] Y. Zhang, T. Ideue, M. Onga, F. Qin, R. Suzuki, A. Zak, R. Tenne, J. Smet, Y. Iwasa, Enhanced intrinsic photovoltaic effect in tungsten disulfide nanotubes, Nature 570 (2019) 349–353, https://doi.org/10.1038/s41586-019-1303-3.
[71] F. Qin, W. Shi, T. Ideue, M. Yoshida, A. Zak, R. Tenne, T. Kikitsu, D. Inoue, D. Hashizume, Y. Iwasa, Superconductivity in a chiral nanotube, Nat. Commun. 8 (2017) 14465, https://doi.org/10.1038/ncomms14465.
[72] I. Kaplan-Ashiri, S.R. Cohen, K. Gartsman, V. Ivanovskaya, T. Heine, G. Seifert, I. Wiesel, H.D. Wagner, R. Tenne, On the mechanical behavior of WS_2 nanotubes under axial tension and compression, Proc. Natl. Acad. Sci. U.S.A. 103 (2006) 523–528, https://doi.org/10.1073/pnas.0505640103.
[73] Y. Feldman, E. Wasserman, D. Srolovitz, R. Tenne, High-rate, gas-phase growth of MoS_2 nested inorganic fullerenes and nanotubes, Science 267 (1995) 222–225, https://doi.org/10.1126/science.267.5195.222.
[74] X. Jia, X. Zhu, W. Tian, Y. Ding, X. Tian, B. Cheng, L. Cheng, S. Bai, Y. Qin, Nanowire templated CVD synthesis and morphological control of MoS_2 nanotubes, J. Mater. Chem. C 8 (2020) 4133–4138, https://doi.org/10.1039/c9tc06060j.
[75] S. Zhuo, Y. Xu, W. Zhao, J. Zhang, B. Zhang, Hierarchical nanosheet-based MoS_2 nanotubes fabricated by an anion-exchange reaction of MoO_3-amine hybrid nanowires, Angew. Chem. Int. Ed. 52 (2013) 8602–8606, https://doi.org/10.1002/anie.201303480.
[76] M. Remškar, A. Mrzel, M. Viršek, A. Jesih, Inorganic nanotubes as nanoreactors: the first MoS_2 nanopods, Adv. Mater. 19 (2007) 4276–4278, https://doi.org/10.1002/adma.200701784.
[77] P. Thangasamy, M. Sathish, Rapid, one-pot synthesis of luminescent MoS_2 nanoscrolls using supercritical fluid processing, J. Mater. Chem. C 4 (2016) 1165–1169, https://doi.org/10.1039/c5tc03630e.
[78] J. Meng, G. Wang, X. Li, X. Lu, J. Zhang, H. Yu, W. Chen, L. Du, M. Liao, J. Zhao, Rolling up a monolayer MoS_2 sheet, Small 12 (2016) 3770–3774, https://doi.org/10.1002/smll.201601413.
[79] K.H. Choi, D.H. Suh, A vacancy-driven phase transition in MoX_2 (X: S, Se and Te) nanoscrolls, Nanoscale 10 (2018) 7918–7926, https://doi.org/10.1039/c7nr08634b.
[80] X. Cui, Z. Kong, E. Gao, D. Huang, Y. Hao, H. Shen, C.-a. Di, Z. Xu, J. Zheng, D. Zhu, Rolling up transition metal dichalcogenide nanoscrolls via one drop of ethanol, Nat. Commun. 9 (2018) 1301, https://doi.org/10.1038/s41467-018-03752-5.
[81] L. Wang, Q. Yue, C. Pei, H. Fan, J. Dai, X. Huang, H. Li, W. Huang, Scrolling bilayer WS_2/MoS $_2$ heterostructures for high-performance photo-detection, Nano Res. 13 (2020) 959–966, https://doi.org/10.1007/s12274-020-2725-9.
[82] B. Zong, Q. Xu, Q. Li, X. Fang, X. Chen, C. Liu, J. Zang, Z. Bo, S. Mao, Novel insights into the unique intrinsic sensing behaviors of 2D nanomaterials for volatile organic compounds: from graphene to MoS_2 and black phosphorous, J. Mater. Chem. A 9 (2021) 14411–14421, https://doi.org/10.1039/d1ta02383g.
[83] M. Weng, M. Zhang, T. Yanase, F. Uehara, T. Nagahama, T. Shimada, Catalytic chemical vapor deposition and structural analysis of MoS_2 nanotubes, Jpn. J. Appl. Phys. 57 (2018) 030304, https://doi.org/10.7567/jjap.57.030304.
[84] O. Brontvein, D.G. Stroppa, R. Popovitz-Biro, A. Albu-Yaron, M. Levy, D. Feuerman, L. Houben, R. Tenne, J.M. Gordon, New high-temperature Pb-catalyzed synthesis of inorganic nanotubes, J. Am. Chem. Soc. 134 (2012) 16379–16386, https://doi.org/10.1021/ja307043w.
[85] H. Kim, S.J. Yun, J.C. Park, M.H. Park, J.H. Park, K.K. Kim, Y.H. Lee, Seed growth of tungsten diselenide nanotubes from tungsten oxides, Small 11 (2015) 2192–2199, https://doi.org/10.1002/smll.201403279.
[86] B. Zhao, Z. Wan, Y. Liu, J. Xu, X. Yang, D. Shen, Z. Zhang, C. Guo, Q. Qian, J. Li, R. Wu, Z. Lin, X. Yan, B. Li, Z. Zhang, H. Ma, B. Li, X. Chen, Y. Qiao, I. Shakir, Z. Almutairi, F. Wei, Y. Zhang, X. Pan, Y. Huang, Y. Ping, X. Duan, X. Duan, High-order superlattices by rolling up van der Waals heterostructures, Nature 591 (2021) 385–390, https://doi.org/10.1038/s41586-021-03338-0.
[87] R. Ghosh, H.I. Lin, Y.S. Chen, M. Singh, Z.L. Yen, S. Chiu, H.Y. Lin, K.P. Bera, Y.M. Liao, M. Hofmann, Y.P. Hsieh, Y.F. Chen, QD/2D hybrid nanoscrolls: a new class of materials for high-performance polarized photodetection and ultralow threshold laser action, Small 16 (2020) 2003944, https://doi.org/10.1002/smll.202003944.
[88] A. Zak, L. Sallacan-Ecker, A. Margolin, M. Genut, R. Tenne, Insight into the growth mechanism of WS_2 nanotubes in the scaled-up fluidized-bed reactor, Nano 4 (2009) 91–98, https://doi.org/10.1142/s1793292009001551.
[89] Q. Zhang, W. Wang, X. Kong, R.G. Mendes, L. Fang, Y. Xue, Y. Xiao, M.H. Rümmeli, S. Chen, L. Fu, Edge-to-Edge oriented self-assembly of ReS_2 nanoflakes, J. Am. Chem. Soc. 138 (2016) 11101–11104, https://doi.org/10.1021/jacs.6b06368.
[90] H.S. Kim, J. Jeong, G.H. Kwon, H. Kwon, M. Baik, M.H. Cho, Improvement of electrical performance using $PtSe_2$/$PtTe_2$ edge contact synthesized by molecular beam epitaxy, Appl. Surf. Sci. 585 (2022) 152507, https://doi.org/10.1016/j.apsusc.2022.152507.
[91] C. Xie, L. Zeng, Z. Zhang, Y.-H. Tsang, L. Luo, J.-H. Lee, High-performance broadband heterojunction photodetectors based on multilayered $PtSe_2$ directly grown on a Si substrate, Nanoscale 10 (2018) 15285–15293, https://doi.org/10.1039/c8nr04004d.
[92] S. Grigoriev, V.Y. Fominski, A. Gnedovets, R.I. Romanov, Experimental and numerical study of the chemical composition of WSe_x thin films obtained by pulsed laser deposition in vacuum and in a buffer gas atmosphere, Appl. Surf. Sci. 258 (2012) 7000–7007, https://doi.org/10.1016/j.apsusc.2012.03.153.
[93] Y. Shi, H. Li, L.J. Li, Recent advances in controlled synthesis of two-dimensional transition metal dichalcogenides via vapour deposition techniques, Chem. Soc. Rev. 44 (2015) 2744–2756, https://doi.org/10.1039/c4cs00256c.
[94] K. Kang, S. Xie, L. Huang, Y. Han, P.Y. Huang, K.F. Mak, C.-J. Kim, D. Muller, J. Park, High-mobility three-atom-thick semiconducting films with wafer-scale homogeneity, Nature 520 (2015) 656–660, https://doi.org/10.1038/nature14417.
[95] Y. Huang, Y.-H. Pan, R. Yang, L.-H. Bao, L. Meng, H.-L. Luo, Y.-Q. Cai, G.-D. Liu, W.-J. Zhao, Z. Zhou, Universal mechanical exfoliation of large-area 2D crystals, Nat. Commun. 11 (2020) 2453, https://doi.org/10.1038/s41467-020-16266-w.
[96] J. Shen, J. Wu, M. Wang, P. Dong, J. Xu, X. Li, X. Zhang, J. Yuan, X. Wang, M. Ye, Surface tension components based selection of cosolvents for efficient liquid phase exfoliation of 2D materials, Small 12 (2016) 2741–2749, https://doi.org/10.1002/smll.201503834.
[97] S.H. Choi, S.J. Yun, Y.S. Won, C.S. Oh, S.M. Kim, K.K. Kim, Y.H. Lee, Large-scale synthesis of graphene and other 2D materials towards industrialization, Nat. Commun. 13 (2022) 1484, https://doi.org/10.1038/s41467-022-29182-y.

[98] L. Zhang, C. Chen, J. Zhou, G. Yang, J. Wang, D. Liu, Z. Chen, W. Lei, Solid phase exfoliation for producing dispersible transition metal dichalcogenides nanosheets, Adv. Funct. Mater. 30 (2020) 2004139, https://doi.org/10.1002/adfm.202004139.
[99] Z.H. Miao, L.X. Lv, K. Li, P.Y. Liu, Z. Li, H. Yang, Q. Zhao, M. Chang, L. Zhen, C.Y. Xu, Liquid exfoliation of colloidal rhenium disulfide nanosheets as a multifunctional theranostic agent for in vivo photoacoustic/CT imaging and photothermal therapy, Small 14 (2018) 1703789, https://doi.org/10.1002/smll.201703789.
[100] A. Giri, H. Yang, K. Thiyagarajan, W. Jang, J.M. Myoung, R. Singh, A. Soon, K. Cho, U. Jeong, One-step solution phase growth of transition metal dichalcogenide thin films directly on solid substrates, Adv. Mater. 29 (2017) 1700291, https://doi.org/10.1002/adma.201700291.
[101] J. Wang, Z. Chen, Y. Wang, T. Wang, S. Liu, G. Chen, Y. Wang, W. Ren, L. Li, Molybdenum disulfide film saturable absorber based on sol-gel glass and spin-coating used in high-power Q-switched Nd: YAG laser, ACS Appl. Mater. Interfaces 12 (2020) 9404−9408, https://doi.org/10.1021/acsami.9b14494.
[102] E. Cairns, A. Ayyagari, C. McCoy, S. Berkebile, D. Berman, S. Aouadi, A.A. Voevodin, Tribological behavior of molybdenum disulfide and tungsten disulfide sprayed coatings in low viscosity hydrocarbon environments, Tribol. Int. 179 (2023) 108206, https://doi.org/10.1016/j.triboint.2022.108206.
[103] T. Nisar, T. Balster, A. Haider, U. Kortz, V. Wagner, Growth of ultra-thin large sized 2D flakes at air-liquid interface to obtain 2D-WS_2 monolayers, J. Phys. Appl. Phys. 54 (2020) 065301, https://doi.org/10.1088/1361-6463/abc198.
[104] X. Zhao, J. Li, S. Mu, W. He, D. Zhang, X. Wu, C. Wang, H. Zeng, Efficient removal of mercury ions with MoS_2-nanosheet-decorated PVDF composite adsorption membrane, Environ. Pollut. 268 (2021) 115705, https://doi.org/10.1016/j.envpol.2020.115705.
[105] Y. Su, Z. Jiang, Y. Wang, H. Zhang, MoS_2 nanosheets supported on anodic aluminum oxide membrane: an effective interface for label-free electrochemical detection of microRNA, Anal. Chim. Acta (2023) 341522, https://doi.org/10.1016/j.aca.2023.341522.
[106] S. Solanki, A. Soni, M.K. Pandey, A. Biradar, G. Sumana, Langmuir-blodgett nanoassemblies of the MoS_2-Au composite at the air-water interface for dengue detection, ACS Appl. Mater. Interfaces 10 (2018) 3020−3028, https://doi.org/10.1021/acsami.7b14391.
[107] D.X. Nghia, J.J. Baek, J.Y. Oh, T.I. Lee, Deformable thermoelectric sponge based on layer-by-layer self-assembled transition metal dichalcogenide nanosheets for powering electronic skin, Ceram. Int. 49 (2023) 9307−9315, https://doi.org/10.1016/j.ceramint.2022.11.097.
[108] D. McManus, S. Vranic, F. Withers, V. Sanchez-Romaguera, M. Macucci, H. Yang, R. Sorrentino, K. Parvez, S.-K. Son, G.J.N.n. Iannaccone, Water-based and biocompatible 2D crystal inks for all-inkjet-printed heterostructures, Nat. Nanotechnol. 12 (2017) 343−350, https://doi.org/10.1038/nnano.2016.281.
[109] J.-Y. Lin, C.-Y. Chan, S.-W. Chou, Electrophoretic deposition of transparent MoS_2-graphene nanosheet composite films as counter electrodes in dye-sensitized solar cells, Chem. Commun. 49 (2013) 1440−1442, https://doi.org/10.1039/c2cc38658e.
[110] G. Ke, H. Chen, J. He, X. Wu, Y. Gao, Y. Li, H. Mi, Q. Zhang, C. He, X. Ren, Ultrathin MoS_2 anchored on 3D carbon skeleton containing SnS quantum dots as a high-performance anode for advanced lithium ion batteries, Chem. Eng. J. 403 (2021) 126251, https://doi.org/10.1016/j.cej.2020.126251.
[111] J. Kibsgaard, Z. Chen, B.N. Reinecke, T.F. Jaramillo, Engineering the surface structure of MoS_2 to preferentially expose active edge sites for electrocatalysis, Nat. Mater. 11 (2012) 963−969, https://doi.org/10.1038/nmat3439.
[112] X. Zuo, K. Chang, J. Zhao, Z. Xie, H. Tang, B. Li, Z. Chang, Bubble-template-assisted synthesis of hollow fullerene-like MoS_2 nanocages as a lithium ion battery anode material, J. Mater. Chem. A 4 (2016) 51−58, https://doi.org/10.1039/c5ta06869j.
[113] C. Li, C. Liu, Y. Wang, Y. Lu, L. Zhu, T. Sun, Drastically-enlarged interlayer-spacing MoS_2 nanocages by inserted carbon motifs as high performance cathodes for aqueous zinc-ion batteries, Energy Storage Mater. 49 (2022) 144−152, https://doi.org/10.1016/j.ensm.2022.03.048.
[114] S. Wei, R. Zhou, G. Wang, Enhanced electrochemical performance of self-assembled nanoflowers of MoS_2 nanosheets as supercapacitor electrode materials, ACS. Omega. 4 (2019) 15780−15788, https://doi.org/10.1021/acsomega.9b01058.
[115] S. Rani, M. Tanwar, M. Sharma, L. Bansal, R. Kumar, R. Bhatia, S. Ivaturi, Enhancing energy storage capabilities of MoS_2 nanoflowers through designing nano-architecture by controlling synthesis growth parameters, J. Energy Storage 58 (2023) 106343, https://doi.org/10.1016/j.est.2022.106343.
[116] M.K. Rajbhar, S. De, G. Sanyal, A. Kumar, B. Chakraborty, S. Chatterjee, Defect-engineered 3D nanostructured MoS_2 for detection of ammonia gas at room temperature, ACS Appl. Nano Mater. 6 (2023) 5284−5297, https://doi.org/10.1021/acsanm.2c05361.
[117] N. Masurkar, N.K. Thangavel, L.M.R. Arava, CVD-grown $MoSe_2$ nanoflowers with dual active sites for efficient electrochemical hydrogen evolution reaction, ACS Appl. Mater. Interfaces 10 (2018) 27771−27779, https://doi.org/10.1021/acsami.8b07489.
[118] C.-B. Ma, X. Qi, B. Chen, S. Bao, Z. Yin, X.-J. Wu, Z. Luo, J. Wei, H.-L. Zhang, H. Zhang, MoS_2 nanoflower-decorated reduced graphene oxide paper for high-performance hydrogen evolution reaction, Nanoscale 6 (2014) 5624−5629, https://doi.org/10.1039/c3nr04975b.
[119] X. Wang, J. Ding, S. Yao, X. Wu, Q. Feng, Z. Wang, B. Geng, High supercapacitor and adsorption behaviors of flower-like MoS_2 nanostructures, J. Mater. Chem. A 2 (2014) 15958−15963, https://doi.org/10.1039/c4ta03044c.
[120] Z. Cheng, Y. Chen, Y. Yang, L. Zhang, H. Pan, X. Fan, S. Xiang, Z. Zhang, Metallic MoS_2 nanoflowers decorated graphene nanosheet catalytically boosts the volumetric capacity and cycle life of lithium−sulfur batteries, Adv. Energy Mater. 11 (2021) 2003718, https://doi.org/10.1002/aenm.202003718.
[121] X. Lu, Y. Lin, H. Dong, W. Dai, X. Chen, X. Qu, X. Zhang, One-step hydrothermal fabrication of three-dimensional MoS_2 nanoflower using polypyrrole as template for efficient hydrogen evolution reaction, Sci. Rep. 7 (2017) 42309, https://doi.org/10.1038/srep42309.
[122] Y. Wang, L. Yu, X.W. Lou, Synthesis of highly uniform molybdenum-glycerate spheres and their conversion into hierarchical MoS_2 hollow nanospheres for lithium-ion batteries, Angew. Chem. Int. Ed. 55 (2016) 7423−7426, https://doi.org/10.1002/anie.201601673.
[123] X. Chen, G. Liu, W. Zheng, W. Feng, W. Cao, W. Hu, P. Hu, Vertical 2D MoO_2/$MoSe_2$ core-shell nanosheet arrays as high-performance electrocatalysts for hydrogen evolution reaction, Adv. Funct. Mater. 26 (2016) 8537−8544, https://doi.org/10.1002/adfm.201603674.
[124] F. Gong, L. Peng, H. Liu, Y. Zhang, D. Jia, S. Fang, F. Li, D. Li, 3D core-shell MoS_2 superspheres composed of oriented nanosheets with quasi molecular superlattices: mimicked embryo formation and Li-storage properties, J. Mater. Chem. A 6 (2018) 18498−18507, https://doi.org/10.1039/c8ta07165a.
[125] W. Wu, J. Wang, Q. Deng, H. Luo, Y. Li, M. Wei, Low crystalline 1T-MoS_2@S-doped carbon hollow spheres as an anode material for Lithium-ion battery, J. Colloid Interface Sci. 601 (2021) 411−417, https://doi.org/10.1016/j.jcis.2021.05.146.
[126] X. Geng, W. Wu, N. Li, W. Sun, J. Armstrong, A. Al-hilo, M. Brozak, J. Cui, T.-p. Chen, Three-dimensional structures of MoS_2 nanosheets with ultrahigh hydrogen evolution reaction in water reduction, Adv. Funct. Mater. 24 (2014) 6123−6129, https://doi.org/10.1002/adfm.201401328.
[127] J. Yang, S. Tang, Q. Yang, Z. Liu, C. Liu, Y. Wu, Z. Li, R. Zhu, W. Jiang, P. He, X. Si, F. Zhang, Z. Liu, Confined growth of 3D ordered, highly curved MoS_2 frameworks for superior lithium-ion storage, Mater. Lett. 347 (2023) 134540, https://doi.org/10.1016/j.matlet.2023.134540.
[128] K. Kang, K.-H. Lee, Y. Han, H. Gao, S. Xie, D.A. Muller, J. Park, Layer-by-layer assembly of two-dimensional materials into wafer-scale heterostructures, Nature 550 (2017) 229−233, https://doi.org/10.1038/nature23905.
[129] S. Seo, S. Kim, H. Choi, J. Lee, H. Yoon, G. Piao, J.C. Park, Y. Jung, J. Song, S.Y. Jeong, H. Park, S. Lee, Direct In Situ Growth of Centimeter-Scale Multi-Heterojunction MoS_2/WS_2/WSe_2 Thin-Film Catalyst for Photo-Electrochemical Hydrogen Evolution, Adv. Sci. 6 (2019) 1900301, https://doi.org/10.1002/advs.201900301.
[130] J. Wang, J. Liu, D. Chao, J. Yan, J. Lin, Z.X. Shen, Self-assembly of honeycomb-like MoS_2 nanoarchitectures anchored into graphene foam for enhanced lithium-ion storage, Adv. Mater. 26 (2014) 7162−7169, https://doi.org/10.1002/adma.201402728.
[131] H. Wang, L. Geng, Z. Zhang, P. Zhong, F. Liu, Y. Xie, Y. Zhao, P. Li, X. Ma, Vertically molybdenum disulfide nanosheets on carbon cloth using CVD by controlling growth atmosphere for electrocatalysis, Nanotechnology 34 (2023) 375601, https://doi.org/10.1088/1361-6528/acd854.
[132] M. Lin, Z.Y. Fu, H.R. Tan, J.P.Y. Tan, S.C. Ng, E. Teo, Hydrothermal synthesis of CeO_2 nanocrystals: ostwald ripening or oriented attachment? Cryst. Growth Des. 12 (2012) 3296−3303, https://doi.org/10.1021/cg300421x.
[133] X. Zhang, X. Huang, M. Xue, X. Ye, W. Lei, H. Tang, C. Li, Hydrothermal synthesis and characterization of 3D flower-like MoS_2 microspheres, Mater. Lett. 148 (2015) 67−70, https://doi.org/10.1016/j.matlet.2015.02.027.
[134] N. Al-Ansi, A. Salah, Q.A. Drmosh, G.D. Yang, A. Hezam, A. Al-Salihy, J. Lin, X.L. Wu, L. Zhao, J.P. Zhang, S.I. Wang, H.Z. Sun, Carbonized polymer dots for controlling construction of MoS_2 flower-like nanospheres to achieve high-performance Li/Na storage devices, Small 19 (2023) 2304459, https://doi.org/10.1002/smll.202304459.
[135] D. Xiao, L. Xiaoke, H. Kang, W. Chuanjie, R. Zhiyan, W. Yongkang, L. Aidong, L. Jia, L. Jianguo, The design strategy of Pt-based electrocatalysts: insights from mass transport of fuel cells, Mater. Today Energy (2024) 101503, https://doi.org/10.1016/j.mtener.2024.101503.
[136] Z. Niu, H. Liu, Z. Qiao, K. Qiao, P. Sun, H. Xu, S. Wang, D. Cao, Yolk-like Pt nanoparticles as cathode catalysts for low-Pt-loading proton-exchange membrane fuel cells, Mater. Today Energy 27 (2022) 101043, https://doi.org/10.1016/j.mtener.2022.101043.
[137] T.B. Ferriday, P.H. Middleton, Alkaline fuel cell technology - a review, Int. J. Hydrogen Energy 46 (2021) 18489−18510, https://doi.org/10.1016/j.ijhydene.2021.02.203.
[138] K. Strickland, R. Pavlicek, E. Miner, Q. Jia, I. Zoller, S. Ghoshal, W. Liang, S. Mukerjee, Anion resistant oxygen reduction electrocatalyst in phosphoric acid fuel cell, ACS Catal. 8 (2018) 3833−3843, https://doi.org/10.1021/acscatal.8b00390.
[139] R.R. Contreras, J. Almarza, L. Rincón, Molten Carbonate Fuel Cells: a Technological Perspective and Review, Energy Sources, Part A: Recovery, Utilization, and Environmental Effects, 2021, pp. 1−15, https://doi.org/10.1080/15567036.2021.2013346.
[140] Z. Lu, H. Daoming, Z. Zidi, L. Fangsheng, D. Dehua, X. Changrong, A coking-tolerance dendritic anode with exceptional power density toward direct

ethanol-fueled solid oxide fuel cells, Mater. Today Energy 34 (2023) 101290, https://doi.org/10.1016/j.mtener.2023.101290.
[141] S. Jinzhi, W. Ruiwen, L. Huidong, Z. Lu, L. Shaoqin, Boosting bioelectricity generation using three-dimensional nitrogen-doped macroporous carbons as freestanding anode, Mater. Today Energy 33 (2023) 101273, https://doi.org/10.1016/j.mtener.2023.101273.
[142] L. Fei, Y. Yonggang, X. Meiying, C. Yuan, L. Wei, 2D covalent organic framework/reduced graphene oxide hybrid hydrogel for simultaneous power generation and organic contamination degradation in microbial fuel cell, Mater. Today Energy 39 (2023) 101464, https://doi.org/10.1016/j.mtener.2023.101464.
[143] A. Yuda, A. Ashok, A. Kumar, A comprehensive and critical review on recent progress in anode catalyst for methanol oxidation reaction, Catal. Rev. 64 (2020) 126–228, https://doi.org/10.1080/01614940.2020.1802811.
[144] G.H. Byun, J.A. Kim, N.Y. Kim, Y.S. Cho, C.R. Park, Molecular engineering of hydrocarbon membrane to substitute perfluorinated sulfonic acid membrane for proton exchange membrane fuel cell operation, Mater. Today Energy 17 (2020) 100483, https://doi.org/10.1016/j.mtener.2020.100483.
[145] C. Liu, X. Wang, J. Xu, C. Wang, H. Chen, W. Liu, Z. Chen, X. Du, S. Wang, Z. Wang, PEMs with high proton conductivity and excellent methanol resistance based on sulfonated poly (aryl ether ketone sulfone) containing comb-shaped structures for DMFCs applications, Int. J. Hydrogen Energy 45 (2019) 945–957, https://doi.org/10.1016/j.ijhydene.2019.10.166.
[146] Y.S. Li, Y.L. He, W.W. Yang, Performance characteristics of air-breathing anion-exchange membrane direct ethanol fuel cells, Int. J. Hydrogen Energy 38 (2013) 13427–13433, https://doi.org/10.1016/j.ijhydene.2013.07.042.
[147] S. Singha, T. Jana, J.A. Modestra, A. Naresh Kumar, S.V. Mohan, Highly efficient sulfonated polybenzimidazole as a proton exchange membrane for microbial fuel cells, J. Power Sources 317 (2016) 143–152, https://doi.org/10.1016/j.jpowsour.2016.03.103.
[148] Y. Karam, G.R. Igal, B. Simon, R.D. Dario, How can we design anion-exchange membranes to achieve longer fuel cell lifetime? J. Membr. Sci. 690 (2023) 122164 https://doi.org/10.1016/j.memsci.2023.122164.
[149] W. Yajie, W. Yannan, G. Maolian, B. Tao, Z. Xiuling, Poly(isatin-piperidinium-terphenyl) anion exchange membranes with improved performance for direct borohydride fuel cells, Int. J. Hydrogen Energy 48 (2023) 14837–14852, https://doi.org/10.1016/j.ijhydene.2022.12.082.
[150] R. Vinodh, R. Atchudan, H.-J. Kim, M. Yi, Recent advancements in polysulfone based membranes for fuel cell (PEMFCs, DMFCs and AMFCs) applications: a critical review, Polymers 14 (2022) 300, https://doi.org/10.3390/polym14020300.
[151] R. Zeng, K. Wang, W. Shao, J. Lai, S. Song, Y. Wang, Investigation on the coordination mechanism of Pt-containing species and qualification of the alkaline content during Pt/C preparation via a solvothermal polyol method, Chin. J. Catal. 41 (2020) 820–829, https://doi.org/10.1016/s1872-2067(19)63456-x.
[152] I. Jiménez-Morales, A. Reyes-Carmona, M. Dupont, S. Cavaliere, M. Rodlert, F. Mornaghini, M.J. Larsen, M. Odgaard, J. Zajac, D.J. Jones, J. Rozière, Correlation between the surface characteristics of carbon supports and their electrochemical stability and performance in fuel cell cathodes, Carbon. Energy. 3 (2021) 654–665, https://doi.org/10.1002/cey2.109.
[153] A.P. Tiwari, D. Kim, Y. Kim, H. Lee, Bifunctional oxygen electrocatalysis through chemical bonding of transition metal chalcogenides on conductive carbons, Adv. Energy Mater. 7 (2017) 1602217, https://doi.org/10.1002/aenm.201602217.
[154] C. Lu, W.-w. Liu, H. Li, B.K. Tay, A binder-free CNT network-MoS_2 composite as a high performance anode material in lithium ion batteries, Chem. Commun. 50 (2014) 3338–3340, https://doi.org/10.1039/c3cc49647c.
[155] C. Zhao, Y. Zhang, L. Chen, C. Yan, P. Zhang, J.M. Ang, X. Lu, Self-assembly-assisted facile synthesis of MoS_2-based hybrid tubular nanostructures for efficient bifunctional electrocatalysis, ACS Appl. Mater. Interfaces 10 (2018) 23731–23739, https://doi.org/10.1021/acsami.8b04140.
[156] Z. Liu, J. Gao, G. Zhang, Y. Cheng, Y.-W. Zhang, From two-dimensional nanosheets to roll-up structures: expanding the family of nanoscroll, Nanotechnology 28 (2017) 385704, https://doi.org/10.1088/1361-6528/aa7bf8.
[157] W.J. Niu, J.Z. He, B.N. Gu, M.C. Liu, Y.L. Chueh, Opportunities and challenges in precise synthesis of transition metal single-atom supported by 2D materials as catalysts toward oxygen reduction reaction, Adv. Funct. Mater. 31 (2021) 2103558, https://doi.org/10.1002/adfm.202103558.
[158] J.-H. Chen, C. Jang, S. Xiao, M. Ishigami, M.S. Fuhrer, Intrinsic and extrinsic performance limits of graphene devices on SiO_2, Nat. Nanotechnol. 3 (2008) 206–209, https://doi.org/10.1038/nnano.2008.58.
[159] D.K. Perivoliotis, Y. Sato, K. Suenaga, N. Tagmatarchis, Covalently functionalized layered MoS_2 supported Pd nanoparticles as highly active oxygen reduction electrocatalysts, Nanoscale 12 (2020) 18278–18288, https://doi.org/10.1039/d0nr04446f.
[160] N.F. Rosli, C.C. Mayorga-Martinez, N.M. Latiff, N. Rohaizad, Z. Sofer, A.C. Fisher, M. Pumera, Layered $PtTe_2$ matches electrocatalytic performance of Pt/C for oxygen reduction reaction with significantly lower toxicity, ACS Sustain. Chem. Eng. 6 (2018) 7432–7441, https://doi.org/10.1021/acssuschemeng.7b04920.
[161] M. Samanta, S. Ghosh, M. Mukherjee, B. Das, C. Bose, K.K. Chattopadhyay, Enhanced electrocatalytic oxygen reduction reaction from organic-inorganic heterostructure, Int. J. Hydrogen Energy 47 (2022) 6710–6720, https://doi.org/10.1016/j.ijhydene.2021.12.067.
[162] Y. Hu, D.H.C. Chua, Synthesizing 2D MoS_2 nanofins on carbon nanospheres as catalyst support for proton exchange membrane fuel cells, Sci. Rep. 6 (2016) 28088, https://doi.org/10.1038/srep28088.
[163] A. Arunchander, S.G. Peera, A.K. Sahu, Synthesis of flower-like molybdenum sulfide/graphene hybrid as an efficient oxygen reduction electrocatalyst for anion exchange membrane fuel cells, J. Power Sources 353 (2017) 104–114, https://doi.org/10.1016/j.jpowsour.2017.03.149.
[164] J. Li, G. Li, J. Wang, C. Xue, X. Li, S. Wang, B. Han, M. Yang, L. Li, A novel core-double shell heterostructure derived from a metal-organic framework for efficient HER, OER and ORR electrocatalysis, Inorg. Chem. Front. 7 (2020) 191–197, https://doi.org/10.1039/c9qi01080g.
[165] D.C. Nguyen, T.L. Luyen Doan, S. Prabhakaran, D.T. Tran, D.H. Kim, J.H. Lee, N.H. Kim, Hierarchical Co and Nb dual-doped MoS_2 nanosheets shelled micro-TiO_2 hollow spheres as effective multifunctional electrocatalysts for HER, OER, and ORR, Nano. Energy. 82 (2021) 105750, https://doi.org/10.1016/j.nanoen.2021.105750.
[166] S.V. Prabhakar Vattikuti, P.C. Nagajyothi, K.C. Devarayapalli, K. Yoo, N. Dang Nam, J. Shim, Hybrid Ag/MoS_2 nanosheets for efficient electrocatalytic oxygen reduction, Appl. Surf. Sci. 526 (2020) 146751, https://doi.org/10.1016/j.apsusc.2020.146751.
[167] S.J. Rowley-Neale, J.M. Fearn, D.A.C. Brownson, G.C. Smith, X. Ji, C.E. Banks, 2D molybdenum disulphide (2D-MoS_2) modified electrodes explored towards the oxygen reduction reaction, Nanoscale 8 (2016) 14767–14777, https://doi.org/10.1039/c6nr04073j.
[168] H. Huang, X. Feng, C. Du, W. Song, High-quality phosphorus-doped MoS_2 ultrathin nanosheets with amenable ORR catalytic activity, Chem. Commun. 51 (2015) 7903–7906, https://doi.org/10.1039/c5cc01841b.
[169] H. Huang, X. Feng, C. Du, S. Wu, W. Song, Incorporated oxygen in MoS_2 ultrathin nanosheets for efficient ORR catalysis, J. Mater. Chem. A 3 (2015) 16050–16056, https://doi.org/10.1039/c5ta01600b.
[170] J. Zhou, H. Xiao, B. Zhou, F. Huang, S. Zhou, W. Xiao, D. Wang, Hierarchical MoS_2-rGO nanosheets with high MoS_2 loading with enhanced electrocatalytic performance, Appl. Surf. Sci. 358 (2015) 152–158, https://doi.org/10.1016/j.apsusc.2015.07.187.
[171] J. Mao, P. Liu, C. Du, D. Liang, J. Yan, W. Song, Tailoring 2D MoS_2 heterointerfaces for promising oxygen reduction reaction electrocatalysis, J. Mater. Chem. A 7 (2019) 8785–8789, https://doi.org/10.1039/c9ta01321k.
[172] D. Roy, K. Panigrahi, B.K. Das, U.K. Ghorui, S. Bhattacharjee, M. Samanta, S. Sarkar, K.K. Chattopadhyay, Boron vacancy: a strategy to boost the oxygen reduction reaction of hexagonal boron nitride nanosheet in hBN-MoS_2 heterostructure, Nanoscale Adv. 3 (2021) 4739–4749, https://doi.org/10.1039/d1na00304f.
[173] K. Zhao, W. Gu, L. Zhao, C. Zhang, W. Peng, Y. Xian, MoS_2/Nitrogen-doped graphene as efficient electrocatalyst for oxygen reduction reaction, Electrochim. Acta 169 (2015) 142–149, https://doi.org/10.1016/j.electacta.2015.04.044.
[174] M.T. Anwar, X. Yan, M.R. Asghar, N. Husnain, S. Shen, L. Luo, X. Cheng, G. Wei, J. Zhang, MoS_2-rGO hybrid architecture as durable support for cathode catalyst in proton exchange membrane fuel cells, Chin. J. Catal. 40 (2019) 1160–1167, https://doi.org/10.1016/s1872-2067(19)63365-6.
[175] S.W. Koh, J. Hu, J. Hwang, P. Yu, Z. Sun, Q. Liu, W. Hong, J. Ge, J. Fei, B. Han, Z. Liu, H. Li, Two-dimensional palladium diselenide for the oxygen reduction reaction, Mater. Chem. Front. 5 (2021) 4970–4980, https://doi.org/10.1039/d0qm01113d.
[176] C. Suresh, S. Mutyala, J. Mathiyarasu, Support interactive synthesis of nanostructured MoS_2 electrocatalyst for oxygen reduction reaction, Mater. Lett. 164 (2016) 417–420, https://doi.org/10.1016/j.matlet.2015.11.052.
[177] C. Lee, S. Ozden, C.S. Tewari, O.K. Park, R. Vajtai, K. Chatterjee, P.M. Ajayan, MoS_2-Carbon nanotube porous 3D network for enhanced oxygen reduction reaction, ChemSusChem 11 (2018) 2960–2966, https://doi.org/10.1002/cssc.201800982.
[178] J. Li, C. Wang, H. Shang, Y. Wang, H. You, H. Xu, Y. Du, Metal-modified $PtTe_2$ nanorods: surface reconstruction for efficient methanol oxidation electrocatalysis, Chem. Eng. J. 424 (2021) 130319, https://doi.org/10.1016/j.cej.2021.130319.
[179] A. Gopalakrishnan, L. Durai, J. Ma, C.Y. Kong, S. Badhulika, Vertically aligned few-layer crumpled MoS_2 hybrid nanostructure on porous Ni foam toward promising binder-free methanol electro-oxidation application, Energy. Fuels. 35 (2021) 10169–10180, https://doi.org/10.1021/acs.energyfuels.1c00957.
[180] C. Zhai, M. Sun, M. Zhu, K. Zhang, Y. Du, Insights into photo-activated electrode for boosting electrocatalytic methanol oxidation based on ultrathin MoS_2 nanosheets enwrapped CdS nanowires, Int. J. Hydrogen Energy 42 (2017) 5006–5015, https://doi.org/10.1016/j.ijhydene.2016.11.035.
[181] M. Chandran, A. Raveendran, M. Vinoba, B.K. Vijayan, M. Bhagiyalakshmi, Nickel-decorated MoS_2/MXene nanosheets composites for electrocatalytic oxidation of methanol, Ceram. Int. 47 (2021) 26847–26855, https://doi.org/10.1016/j.ceramint.2021.06.093.
[182] L. Yuwen, F. Xu, B. Xue, Z. Luo, Q. Zhang, B. Bao, S. Su, L. Weng, W. Huang, L. Wang, General synthesis of noble metal (Au, Ag, Pd, Pt) nanocrystal modified MoS_2 nanosheets and the enhanced catalytic activity of Pd-MoS_2 for methanol oxidation, Nanoscale 6 (2014) 5762–5769, https://doi.org/10.1039/c3nr06084e.
[183] M.B. Askari, P. Salarizadeh, Ultra-small ReS_2 nanoparticles hybridized with rGO as cathode and anode catalysts towards hydrogen evolution reaction and methanol electro-oxidation for DMFC in acidic and alkaline media,

Synth. Met. 256 (2019) 116131, https://doi.org/10.1016/j.synthmet.2019.116131.
[184] S. Su, C. Zhang, L. Yuwen, X. Liu, L. Wang, C. Fan, L. Wang, Uniform Au@Pt core-shell nanodendrites supported on molybdenum disulfide nanosheets for the methanol oxidation reaction, Nanoscale 8 (2016) 602–608, https://doi.org/10.1039/c5nr06077j.
[185] X. Zhu, X. Tong, Z. Li, Q. Bian, Y.E.,P. Chen, L. Li, K. Qian, Atomically embedded synergetic dual-metal catalysis FeO&MoS_2 nanoparticles on sodalite structural zeolite toward electrochemical methanol oxidation reaction, Chem. Eng. J. 471 (2023) 144632, https://doi.org/10.1016/j.cej.2023.144632.
[186] L. He, S. Huang, Y. Liu, M. Wang, B. Cui, S. Wu, J. Liu, Z. Zhang, M. Du, Multicomponent Co_9S_8@MoS_2 nanohybrids as a novel trifunctional electrocatalyst for efficient methanol electrooxidation and overall water splitting, J. Colloid Interface Sci. 586 (2021) 538–550, https://doi.org/10.1016/j.jcis.2020.10.119.
[187] B. Tang, Y. Lv, J. Du, Y. Dai, S. Pan, Y. Xie, J. Zou, MoS_2-Coated Ni_3S_2 nanorods with exposed {110} high-index facets as excellent CO-tolerant cocatalysts for Pt: ultradurable catalytic activity for methanol oxidation, ACS Sustain. Chem. Eng. 7 (2019) 11101–11109, https://doi.org/10.1021/acssuschemeng.8b06855.
[188] B. Tang, Y. Lin, Z. Xing, Y. Duan, S. Pan, Y. Dai, J. Yu, J. Zou, Porous coral reefs-like MoS_2/nitrogen-doped bio-carbon as an excellent Pt support/co-catalyst with promising catalytic activity and CO-tolerance for methanol oxidation reaction, Electrochim. Acta 246 (2017) 517–527, https://doi.org/10.1016/j.electacta.2017.06.052.
[189] Q. Zhang, Y. Li, H. He, H. Huang, Building 3D interconnected MoS_2 nanosheet-graphene networks decorated with Rh nanoparticles for boosted methanol oxidation reaction, ACS Sustain. Chem. Eng. 10 (2022) 8940–8948, https://doi.org/10.1021/acssuschemeng.2c02455.
[190] Y. Liu, B. Hu, S. Wu, M. Wang, Z. Zhang, B. Cui, L. He, M. Du, Hierarchical nanocomposite electrocatalyst of bimetallic zeolitic imidazolate framework and MoS_2 sheets for non-Pt methanol oxidation and water splitting, Appl. Catal. B Environ. 258 (2019) 117970, https://doi.org/10.1016/j.apcatb.2019.117970.
[191] K. Feng, B. Tang, P. Wu, Selective growth of MoS_2 for proton exchange membranes with extremely high selectivity, ACS Appl. Mater. Interfaces 5 (2013) 13042–13049, https://doi.org/10.1021/am403946z.
[192] K. Divya, D. Rana, M.S. Sri Abirami Saraswathi, S.D. Bhat, A. Shukla, A. Nagendran, Investigation of the versatility of SPES membranes customized with sulfonated molybdenum disulfide nanosheets for DMFC applications, Int. J. Hydrogen Energy 45 (2020) 15507–15520, https://doi.org/10.1016/j.ijhydene.2020.04.019.
[193] F. Zhong, Z. Zeng, Y. Liu, R. Hou, X. Nie, Y. Jia, J. Xi, H. Liu, W. Niu, F. Zhang, Modification of sulfonated poly (etherether ketone) composite polymer electrolyte membranes with 2D molybdenum disulfide nanosheet-coated carbon nanotubes for direct methanol fuel cell application, Polymer 249 (2022) 124839, https://doi.org/10.1016/j.polymer.2022.124839.
[194] P. Kumar, P. Das, Development of sulfonated poly(vinyl alcohol)/MoS_2-based robust composite proton exchange membranes with higher selectivity, ACS Appl. Polym. Mater. 5 (2023) 8459–8473, https://doi.org/10.1021/acsapm.3c01582.
[195] X. Jiang, Y. Sun, H. Zhang, L. Hou, Preparation and characterization of quaternized poly(vinyl alcohol)/chitosan/MoS_2 composite anion exchange membranes with high selectivity, Carbohydr. Polym. 180 (2018) 96–103, https://doi.org/10.1016/j.carbpol.2017.10.023.